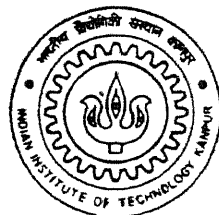


9710514

SIMULATION OF 3-DIMENSIONAL FLUID FLOW IN COMPLEX GEOMETRIES

By
VINOD JUJARE

TH
ME/1998/M
J9368



DEPARTMENT OF MECHANICAL ENGINEERING
INDIAN INSTITUTE OF TECHNOLOGY, KANPUR

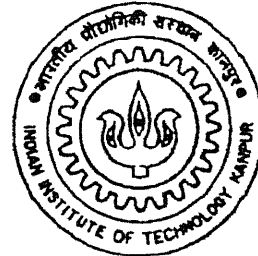
DECEMBER, 1998

SIMULATION OF 3-DIMENSIONAL FLUID FLOW IN COMPLEX GEOMETRIES

A Thesis Submitted
in Partial Fulfilment of the Requirements
for the Degree of

MASTER OF TECHNOLOGY

by
VINOD JUJARE



to the
DEPARTMENT OF MECHANICAL ENGINEERING
INDIAN INSTITUTE OF TECHNOLOGY KANPUR
December, 1998

19 MAY 1999 /ME

TH

ME/1999/10

3-25-28

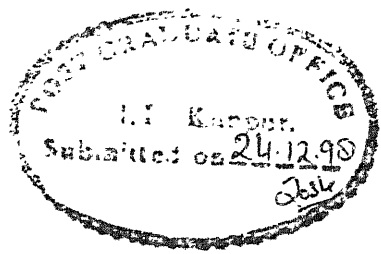
CENTRAL LIBRARY

I.I.T., KANPUR

A 127940



A127940



Certificate

It is certified that the work contained in the thesis entitled **Simulation of 3-Dimensional Fluid Flow In Complex Geometries**, by Vinod Jujare, has been carried out under my supervision and that this work has not been submitted elsewhere for a degree.

A handwritten signature in black ink, appearing to read "Eswaran".

Dr. Vinayak Eswaran
Associate Professor
Department of Mechanical Engineering
I.I.T., Kanpur

December, 1998

Acknowledgements

With a profound sense of gratitude, I express my sincere thanks to my teacher and guide **Prof. V. Eswaran** for his guidance through out the course of this work. He introduced me into the area of CFD and provided me an insight into it. Only because of his constant help, patient guidance and encouragement, I have been able to complete this work. I am greatful to him for all that he has done for me during my stay here.

I express my special thanks to my friends Janardhan, Sarath, Deshmukh, Partho and Tariq for their active support during the course of this work.

I have no words to express my thanks to my parents who have been constant source of inspiration to me. I wish to thank all my friends and well wishers who made my stay at IIT, K memorable and pleasant.

Vinod Jujare

Abstract

Flows in 3D complex geometries mainly curved ducts with square and circular cross sections are studied using a finite volume formulation. The finite volume formulation uses a collocated grid arrangement with cartesian components of velocity, and momentum interpolation to avoid pressure-velocity decoupling. The numerical computations are carried out for 90° and 180° bends of square cross section and a 90° bend of circular cross section. For a range of curvature ratios (R/d) and Reynolds numbers, axial (U_ϕ) and secondary velocities (U_r) are plotted and compared with experimental results of established repute. In all cases, the computed and experimental results are close, and validate the accuracy and robustness of the Navier Stokes solver.

Contents

Abstract	i
Contents	ii
List of Figures	iv
1 Introduction	1
2 Finite - Volume Formulation	5
2.1 Governing Equations	5
2.2 Description of the Finite-Volume	6
2.2.1 Surface areas and Volume	8
2.3 Discretization Procedure	9
2.3.1 Continuity Equation	9
2.3.2 Discretization of General Equation	10
2.4 Semi-Explicit Method	16
2.4.1 Semi-Explicit Time-Stepping	16
2.5 Pressure - Velocity Corrections	17
2.6 Initial and Boundary Conditions	20

3	Results and Discussion	21
3.1	Flow In Curved Ducts	21
3.2	Flow In A 90^0 Bend Square Curved Duct	22
3.2.1	Problem Description	22
3.2.2	Results	23
3.3	Flow In A 180^0 Bend Square Curved Duct	31
3.3.1	Problem Description	31
3.3.2	Results	32
3.4	Flow In A 90^0 Bend Circular Duct	39
3.4.1	Problem Description	39
3.4.2	Results	41
4	Conclusion	50
	Bibliography	51

List of Figures

2.1	Three-dimensional control volume	7
2.2	Face Representation	14
3.1	Schematic of 90^0 bend square duct	23
3.2	Velocity vectors in the symmetry plane of a 90^0 bend duct	24
3.3	Velocity contours in the 90^0 bend flow at (a) $\phi=0^0$, (b) $\phi=30^0$.	25
3.4	Velocity contours in the 90^0 bend flow at (c) $\phi=60^0$, (d) $\phi=90^0$.	26
3.5	The present results in comparison with ref[10] (a) 0^0 , (b) 30^0 , (c) 60^0 , (d) 90^0	27
3.6	Vector plots of secondary velocity at (a) $\phi=0^0$, (b) $\phi=90^0$	28
3.7	Vector plots of secondary velocity at : (c) 9.0 d, (d) 15.75 d . .	29
3.8	Measured(+) and computed friction coefficients at the center-line of the inside and outside curved walls of the bend.	30
3.9	Schematic of 180^0 bend square duct	31
3.10	Streamwise velocity development in the bend shown as velocity vectors plotted in the $x-y$ plane of symmetry.	33
3.11	Mainstream velocity as a function of the radial location r at $z=0.5$ (a) $\phi=36^0$, (b) $\phi=54^0$	34

3.12 Mainstream velocity as a function of the radial location r at $z=0.5$ (c) $\phi=72^0$, (d) $\phi=90^0$	35
3.13 Mainstream velocity as a function of the radial location r at $z=0.5$ (e) $\phi=108^0$, (f) $\phi=126^0$	36
3.14 Mainstream velocity as a function of the radial location r at $z=0.5$ (g) $\phi=144^0$, (h) $\phi=162^0$	37
3.15 Two dimensional vector profiles of the secondary velocities at $\phi=162^0$	38
3.16 (a)Co-Ordinates of the bend (b) Grid Implemented	40
3.17 Development of the axial flow in the plane of symmetry	41
3.18 Development of the axial flow represented by isovelocity contours at (a) $\phi=0^0$, (b) $\phi=12^0$	43
3.19 Development of the axial flow represented by isovelocity contours at (c) $\phi=22.5^0$, (d) $\phi=40.5^0$	44
3.20 Development of the axial flow represented by isovelocity contours at (e) $\phi=58.5^0$, (f) $\phi=82.5^0$	45
3.21 Comparison of the isovelocity contours between the present results and experimental[15]. The upper half domain corresponds to the experimental and the lower half the present results. O, Outer bend; I, Inner bend	46
3.22 Development of secondary flow represented by vector plots at (a) $\phi=4.5^0$, (b) $\phi=12^0$	47
3.23 Development of secondary flow represented by vector plots at (c) $\phi=22.5^0$, (d) $\phi=40.5^0$	48
3.24 Development of secondary flow represented by vector plots at (e) $\phi=58.5^0$, (f) $\phi=82.5^0$	49

Chapter 1

Introduction

The prediction of incompressible fluid flow is needed in almost every branch of engineering. Examples include chemical processing plants, nuclear reactors, heating and ventilation of rooms, cooling of electronic equipments, meteorology, turbomachines, ground water flows, etc. As the field of computational fluid dynamics continues to mature, there is a need of exploiting the most recent advances in numerical mathematics, computing architectures and hardware to solve fluid flow problems of increasing complexity, for industry and in fundamental research.

Successfully obtaining physically meaningful solutions from numerical flow predictions depends on (a) the correctness of the mathematical approximations in the modeling of the physical systems, and (b) the accuracy and efficiency of the numerical scheme and its ability to handle the complexity of the flow geometries under consideration.

The choice of an appropriate numerical method often depends upon the geometry of the flow domain. The most commonly used solution methodologies

are finite-difference, finite-volume and finite-element methods. Both finite-volume and finite-element methods belong to the class of weighted residual methods[1]. However, in implementation, finite-volume discretizations more closely resemble finite-difference methods. Finite-difference methods[1], in general, are algorithmically simplest, while finite-elements[2] are the most flexible with regards to flow geometry, but are rather involved algorithmically. The finite-volume method is often seen as a good compromise between the two – being simpler to implement than the finite-element method and being more suitable for complex domains than the finite-difference method. The finite-volume method has the additional advantages of discretizing the conservation form of the governing equations. This implies that the descretised equations preserve the conservation laws. This is a particular advantage when obtaining accurate solutions for internal flows or flows with shocks.

If the geometry is rectangular then finite-difference methods are often preferred for their simplicity. However, with the growing use of CFD in industrial applications, computations are done for increasingly complex geometries. The recent advances in grid generation techniques[3, 4, 5] allow the use of boundary-fitted grids which permit selective refinement near the boundary walls, etc., and thus reduce storage, computational time, and improve accuracy. However finite-difference schemes used on body-fitted coordinates require us to map the complex domain onto a regular rectangular grid in which transformed equations are solved. This could be global mapping, i.e., mapping the entire flow domain onto a simpler computational domain, or, more commonly, local mapping, i.e., mapping each successive grid point and its related neighbours onto a succession of small and simple domains. The transformation approach is often adopted even for finite-volume schemes.

The most commonly used grids for finite-difference and finite-volume

methods are either staggered or non-staggered (collocated) grids. The staggered grid arrangement is quiet robust and efficient in orthogonal grid computations and avoids pressure-velocity decoupling associated with non-staggered grids. On uniform grids, the grid points have a simple relationship with the grid index and their locations need not be stored. However, on non-uniform grids, the coordinates of each grid point need to be stored. On such grids, a staggered system will store many times more information than non-staggered ones, as each component of velocity and the pressure have different locations in the former. In addition, the grid transformation parameters for each variable is different on staggered grids, and again need to be stored. This also poses problems in the discretization of the non-linear terms on a non-uniform mesh. All this is heavy price to pay for the staggered grid's pre-eminent advantage — the avoidance of pressure-velocity decoupling.

On the other hand, the collocated grid arrangement stores all the dependent variables at the same grid points and only one set of grid relations needs to be considered. This arrangement is susceptible to pressure-velocity decoupling, but this can be avoided by using momentum interpolation[6]. In view of the above considerations, the collocated grid arrangement seems preferable for fluid flow calculations in complex geometries.

In this thesis we attempt to solve incompressible 3-D flows in complex geometries using finite volume formulation that was developed for DRDL, Hyderabad, as part of a project. It has been thoroughly tested for 2-D and 3-D regular geometries. This thesis validates the code for complex 3-D geometries. The finite volume formulation is described in the next chapter. The scheme uses a pressure based primitive variable formulation and general hexahedral elements which can be used to represent complicated computational domains. A collocated grid arrangement is chosen for the storage of the de-

Introduction

pendent variables to facilitate calculation in complex domains. The problem of pressure-velocity decoupling is avoided using momentum interpolation. The Cartesian components of velocity and pressure are used as dependent variables.

Chapter 2

Finite - Volume Formulation

The finite volume formulation presented below has been developed by Dr.V.Eswaran and co-workers as part of a project for DRDL, Hyderabad. The full details are given in the project report[7].

2.1 Governing Equations

The three-dimensional Navier-Stokes equations for laminar flow for an arbitrary spatial region of control volume V bounded by a closed surface S can be expressed in the following general convection-diffusion-source integral form:

$$\frac{\partial}{\partial t} \int_V \rho dV + \int_S \rho \mathbf{u} \cdot d\mathbf{S} = 0 \quad (2.1)$$

$$\frac{\partial}{\partial t} \int_V \rho \phi dV + \int_S [\rho \mathbf{u} \phi - \Gamma_\phi \nabla \phi] \cdot d\mathbf{S} = \int_V S_\phi dV \quad (2.2)$$

where ρ represents the fluid density, \mathbf{u} is the fluid velocity, ϕ stands for any vector component or scalar quantity, S_ϕ is the volumetric source term.

For incompressible flow of Newtonian fluid, the equations takes the form

$$\int_S \mathbf{u} \cdot d\mathbf{S} = 0 \quad (2.3)$$

$$\frac{\partial}{\partial t} \int_V \phi dV + \int_S [u\phi - \frac{\Gamma_\phi}{\rho} \nabla \phi] \cdot dS = \frac{1}{\rho} \int_V S_\phi dV \quad (2.4)$$

and the source term for momentum equations becomes $- \frac{1}{\rho} \int_S p \mathbf{I} \cdot d\mathbf{S}$ where \mathbf{I} is the unit tensor.

In this formulation we work with cartesian components of velocity. So ϕ can be the three cartesian components of velocity u, v, w , as well as any scalar e.g., temperature, which needs to be determined.

2.2 Description of the Finite-Volume

Figure 1 shows the kind of control volume used, with eight vertices but otherwise irregular.

The conservation equations are discretized by employing the general finite-volume approach. The solution domain is subdivided into a number of contiguous (finite) control volumes. The control volumes are defined by the coordinates of their vertices which are assumed to be connected by straight lines. The coordinates of the control volume vertices are calculated by some grid generation procedure. A **Collocated Grid** arrangement is employed, i.e., all the dependent variables (u, v, w, p) are defined at the same location, the centroid of the control volume in Figure 1. The six neighbouring control volume centers are indicated by E, W, N, S, T, and B (for the east, west, north, south, top and bottom neighbours). The face center points e, w, n, s, t, and b are located at the corresponding face centroids of control volume P. Note the edge-centers te, be, ne, se, etc. which are also needed in the computations.

Before the time-stepping can proceed all geometrical parameters need to be computed as part of the investigation. These parameters include the surface vectors for each of the six faces e, w, n, s, t, b of each finite volume and also its volume. These computations can be done by the methods shown below.

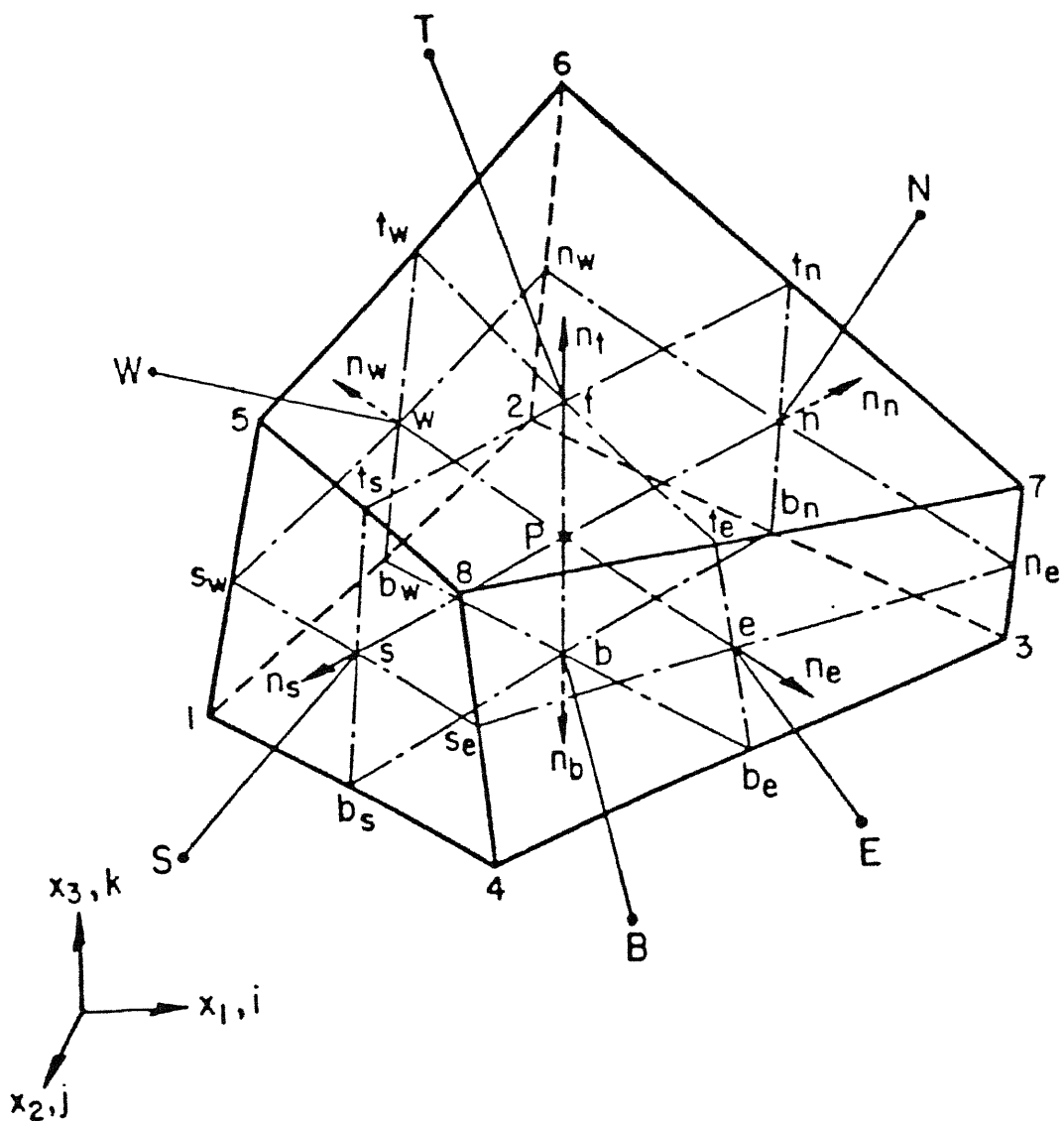


Figure 2.1: Three-dimensional control volume

2.2.1 Surface areas and Volume

The finite volume vertices are numbered 1 to 8 in the manner shown in figure 1. The **outward** surface normals and volume can be found in the following manner suggested by Kordulla and Vinokur[8].

Defining $\mathbf{r}_{ij} = \mathbf{r}_i - \mathbf{r}_j$, where $\mathbf{r}_i, \mathbf{r}_j$ are the position vectors of points i and j respectively, we have for

- East face

$$\mathbf{S}_e = \frac{1}{2}(\mathbf{r}_{74} \times \mathbf{r}_{83}) \quad (2.5)$$

- West face

$$\mathbf{S}_w = \frac{1}{2}(\mathbf{r}_{16} \times \mathbf{r}_{52}) \quad (2.6)$$

- North face

$$\mathbf{S}_n = \frac{1}{2}(\mathbf{r}_{27} \times \mathbf{r}_{63}) \quad (2.7)$$

- South face

$$\mathbf{S}_s = \frac{1}{2}(\mathbf{r}_{18} \times \mathbf{r}_{45}) \quad (2.8)$$

- Top face

$$\mathbf{S}_t = \frac{1}{2}(\mathbf{r}_{75} \times \mathbf{r}_{68}) \quad (2.9)$$

- Bottom face

$$\mathbf{S}_b = \frac{1}{2}(\mathbf{r}_{13} \times \mathbf{r}_{24}) \quad (2.10)$$

The volume of the control cell is calculated from the cell corner coordinates assuming that the cell corners are joined by linear segments to form the six cell faces.

$$V = \frac{1}{3}\mathbf{r}_{71} \cdot (\mathbf{S}_s + \mathbf{S}_b + \mathbf{S}_w) \quad (2.11)$$

2.3 Discretization Procedure

All the conservation equations have the same general form, represented by

$$\frac{\partial}{\partial t} \int_V \rho \phi dV + \int_S [\rho \mathbf{u} \phi - \Gamma_\phi \nabla \phi] \cdot d\mathbf{S} = \int_V S_\phi dV \quad (2.12)$$

The main steps of the discretization procedure to calculate convection and diffusion fluxes and source terms are outlined below. The rate of change and source terms are integrated over the cell volume, whereas the convection and diffusion terms form the sum of fluxes through the CV faces.

2.3.1 Continuity Equation

Equation (2.3) is discretized in the following way.

$$\int_S \rho \mathbf{u} \cdot d\mathbf{S} \approx \sum_{j=e,w,n,s,t,b} \rho (\mathbf{u} \cdot \mathbf{S})_j = \sum_j \rho \mathbf{u}_j \cdot \mathbf{S}_j \quad (2.13)$$

where \mathbf{S}_j is the surface vector representing the area of the j^{th} cell face and \mathbf{u}_j is the velocity defined at the face center j .

In discretized form the continuity equation follows

$$\sum_j F_j = F_e + F_w + F_n + F_s + F_t + F_b = 0 \quad (2.14)$$

where the F_j is the outward mass flux through face j , defined by

$$F_j = \rho \mathbf{u}_j \cdot \mathbf{S}_j$$

2.3.2 Discretization of General Equation

(a) Rate of change

The value of the dependent variable ϕ at the centroid of the control volume (the geometric center) represents an average over the CV as a whole. Thus

$$\frac{\partial}{\partial t} \int_V \rho \phi dV \approx \frac{(\rho \phi V)_P^{n+1} - (\rho \phi V)_P^n}{\Delta t} \approx \rho V \frac{\phi_P^{n+1} - \phi_P^n}{\Delta t} \quad (2.15)$$

where V is the volume of the cell.

(b) Convection fluxes

The surface integral over convection flux of variable ϕ can be approximated in the following form

$$\begin{aligned} \int_S \rho \mathbf{u} \cdot \mathbf{S} \phi \cdot d\mathbf{S} &\approx \sum_j \rho \phi_j (\mathbf{u} \cdot \mathbf{S})_j, \\ &= \sum_j F_j \phi_j \end{aligned} \quad (2.16)$$

where ϕ_j is the value of ϕ at the center of face j . Thus

$$\int_S \rho \mathbf{u} \cdot \mathbf{S} \phi \cdot d\mathbf{S} \approx F_e \phi_e + F_w \phi_w + F_n \phi_n + F_s \phi_s + F_t \phi_t + F_b \phi_b \quad (2.17)$$

where ϕ_e is the (interpolated) value of the variable ϕ at the east face center, etc. This can be evaluated by using a 'center difference' linear interpolation between the neighbouring nodal values ϕ_P and ϕ_E . At east face the value of ϕ_e is given by

$$\phi_e = \frac{V_E}{V_E + V_P} \phi_P + \frac{V_P}{V_E + V_P} \phi_E \quad (2.18)$$

where V_E and V_P are volumes of the cells around the points E and P respectively and ϕ_E and ϕ_P are the values of the dependent variable at these points. Since all dependent variables are defined at the same location, exactly the same interpolation scheme is used to express all of them at the interfaces. However to use the center difference approximation above to compute the convection fluxes may lead to numerical stability problems. Therefore the convection flux

is split into a first-order upwind differencing scheme (UDS), and another part, which equals the difference between the central difference scheme (CDS) and UDS approximations:

$$F_e \phi_e = (F_e \phi_e)^{UDS} + \gamma [(F_e \phi_e)^{CDS} - (F_e \phi_e)^{UDS}] \quad (2.19)$$

The upwind differencing scheme is based on the assumption that the convected cell face value is equal to that at the upstream cell along the same coordinate direction. Thus, the value ϕ_e at the east face is assigned the value ϕ_P if $u_e \geq 0$, i.e., the flux F_e is positive, and the value ϕ_E if $u_e < 0$, i.e., the flux F_e is negative. This can be conveniently summarized as

$$\begin{aligned} F_e \phi_e = & \phi_P [[F_e, 0]] - \phi_E [[-F_e, 0]] + \gamma \left\{ F_e \left(\frac{V_E}{V_E + V_P} \phi_P + \frac{V_P}{V_E + V_P} \phi_E \right) \right. \\ & \left. - \phi_P [[F_e, 0]] + \phi_E [[-F_e, 0]] \right\} \end{aligned} \quad (2.20)$$

Here $[[p, q]]$ denotes the maximum of p and q . Similar expressions can be written for rest of the faces

$$\begin{aligned} F_w \phi_w = & \phi_P [[F_w, 0]] - \phi_W [[-F_w, 0]] + \gamma \left\{ F_w \left(\frac{V_P}{V_W + V_P} \phi_W + \frac{V_W}{V_W + V_P} \phi_P \right) \right. \\ & \left. - \phi_P [[F_w, 0]] + \phi_W [[-F_w, 0]] \right\} \end{aligned} \quad (2.21)$$

$$\begin{aligned} F_n \phi_n = & \phi_P [[F_n, 0]] - \phi_N [[-F_n, 0]] + \gamma \left\{ F_n \left(\frac{V_N}{V_P + V_N} \phi_P + \frac{V_P}{V_P + V_N} \phi_N \right) \right. \\ & \left. - \phi_P [[F_n, 0]] + \phi_N [[-F_n, 0]] \right\} \end{aligned} \quad (2.22)$$

$$\begin{aligned} F_s \phi_s = & \phi_P [[F_s, 0]] - \phi_S [[-F_s, 0]] + \gamma \left\{ F_s \left(\frac{V_P}{V_S + V_P} \phi_S + \frac{V_S}{V_S + V_P} \phi_P \right) \right. \\ & \left. - \phi_P [[F_s, 0]] + \phi_S [[-F_s, 0]] \right\} \end{aligned} \quad (2.23)$$

$$\begin{aligned} F_t \phi_t = & \phi_P [[F_t, 0]] - \phi_T [[-F_t, 0]] + \gamma \left\{ F_t \left(\frac{V_T}{V_P + V_T} \phi_P + \frac{V_P}{V_P + V_T} \phi_T \right) \right. \\ & \left. - \phi_P [[F_t, 0]] + \phi_T [[-F_t, 0]] \right\} \end{aligned} \quad (2.24)$$

$$\begin{aligned} F_b \phi_b = & \phi_P [[F_b, 0]] - \phi_B [[-F_b, 0]] + \gamma \left\{ F_b \left(\frac{V_P}{V_B + V_P} \phi_B + \frac{V_B}{V_B + V_P} \phi_P \right) \right. \\ & \left. - \phi_P [[F_b, 0]] + \phi_B [[-F_b, 0]] \right\} \end{aligned} \quad (2.25)$$

If a fully implicit method is used for time-stepping, the upwind parts of the above equations are 'implicit' in that they are incorporated in the coefficients of

the unknown velocity during the pressure-velocity iterations. The CDS terms on the other hand are evaluated using previous iteration values and used as source term on the right hand side of the same equation. This is the so-called ‘deferred correction’ approach of Khosla and Rubin[9]. Multiplication of the explicit part by a factor γ ($0 \leq \gamma \leq 1$) allows the introduction of numerical diffusion. ($\gamma = 0$ means pure UDS, $\gamma = 1$ means pure CDS). The deferred correction approach enhances the diagonal dominance of the coefficient matrix, which adds to the stability of the solution algorithm.

(c) Diffusion fluxes

The diffusion flux of variable ϕ through the cell faces can be evaluated as follows

$$\int_S \Gamma_\phi \nabla \phi \cdot dS \approx \sum_{j=\epsilon,u,n,s,t,b} (\Gamma_\phi \nabla \phi \cdot S)_j = \sum_j -F_j^d \quad (2.26)$$

For any face we can write

$$S_j = \alpha_1 n^1 + \alpha_2 n^2 + \alpha_3 n^3 \quad (2.27)$$

where n^1 , n^2 and n^3 are any three linearly independent (not necessarily orthogonal) unit vectors. Therefore

$$\begin{aligned} \nabla \phi \cdot S_j &= \nabla \phi \cdot (\alpha_1 n^1 + \alpha_2 n^2 + \alpha_3 n^3) \\ &= \alpha_1 \nabla \phi \cdot n^1 + \alpha_2 \nabla \phi \cdot n^2 + \alpha_3 \nabla \phi \cdot n^3 \end{aligned} \quad (2.28)$$

If $\Delta\phi^1, \Delta\phi^2, \Delta\phi^3$ are the differences in ϕ between the two ends of the line segments $\Delta x^1, \Delta x^2, \Delta x^3$, then

$$\Delta\phi^1 = \nabla \phi \cdot \Delta x^1, \quad \Delta\phi^2 = \nabla \phi \cdot \Delta x^2, \quad \Delta\phi^3 = \nabla \phi \cdot \Delta x^3 \quad (2.29)$$

If furthermore $\Delta x^1, \Delta x^2, \Delta x^3$ are in the directions of n^1, n^2 and n^3 respectively, then it follows from equation (2.29) that

$$\frac{\Delta\phi^1}{\Delta x^1} = \nabla \phi \cdot n^1, \quad \frac{\Delta\phi^2}{\Delta x^2} = \nabla \phi \cdot n^2, \quad \frac{\Delta\phi^3}{\Delta x^3} = \nabla \phi \cdot n^3 \quad (2.30)$$

where Δx^1 , etc. are the magnitudes of $\Delta \mathbf{x}^1$ etc. Consequently we can write, using (2.29) and (2.30)

$$\nabla \phi \cdot \mathbf{S} = \alpha_1 \frac{\Delta \phi^1}{\Delta x^1} + \alpha_2 \frac{\Delta \phi^2}{\Delta x^2} + \alpha_3 \frac{\Delta \phi^3}{\Delta x^3} \quad (2.31)$$

To get α_1, α_2 and α_3 , we express

$$\begin{aligned} \mathbf{n}^1 &= (n_{11} \ n_{12} \ n_{13}) \\ \mathbf{n}^2 &= (n_{21} \ n_{22} \ n_{23}) \\ \mathbf{n}^3 &= (n_{31} \ n_{32} \ n_{33}) \end{aligned} \quad (2.32)$$

where n_{11}, n_{12}, n_{13} are the cartesian components of \mathbf{n} and which can be easily determined by $\frac{\Delta \mathbf{x}_1^1}{\Delta x^1}, \frac{\Delta \mathbf{x}_2^1}{\Delta x^1}, \frac{\Delta \mathbf{x}_3^1}{\Delta x^1}$, where $\Delta \mathbf{x}_1^1, \Delta \mathbf{x}_2^1, \Delta \mathbf{x}_3^1$ are the three components of vector $\Delta \mathbf{x}^1$, etc. The other values $n_{21}..n_{33}$ can be similarly determined. Therefore, equation 2.27 can be written as

$$\begin{bmatrix} n_{11} & n_{12} & n_{13} \\ n_{21} & n_{22} & n_{23} \\ n_{31} & n_{32} & n_{33} \end{bmatrix} \begin{Bmatrix} \alpha_1 \\ \alpha_2 \\ \alpha_3 \end{Bmatrix} = \begin{Bmatrix} S_{1j} \\ S_{2j} \\ S_{3j} \end{Bmatrix} \quad (2.33)$$

where S_{1j}, S_{2j}, S_{3j} are the cartesian components of the surface vector \mathbf{S}_j .

Using Cramer's rule

$$\alpha_1 = \frac{D_1}{D}, \quad \alpha_2 = \frac{D_2}{D}, \quad \alpha_3 = \frac{D_3}{D} \quad (2.34)$$

where D is the determinant of the coefficient matrix. D_1 is obtained by replacing the first column of D by the column with elements S_{1j}, S_{2j}, S_{3j} , etc., we can get $\alpha_1, \alpha_2, \alpha_3$.

The diffusion flux is made of two distinct parts: normal diffusion and cross-derivative diffusion. The second part arises from the nonorthogonality of the grid. The normal derivative diffusion flux of ϕ through any cell face involves the values of ϕ at cell centers whereas the cross-derivative diffusion flux takes into account the edge center values of ϕ . (The normal derivative diffusion flux

is treated implicitly and is coupled with the implicit part of the convective flux to calculate the main coefficients of the discretized equations while the cross-derivative diffusion flux is treated explicitly to avoid the possibility of producing negative coefficients in an implicit treatment. This term together with explicit part of convective flux is added to the source term). The example of the east face is taken to illustrate the diffusion model. Given the edge center values $\phi_{te}, \phi_{be}, \phi_{se}, \phi_{ne}$ we can get the normal diffusion term $\frac{\phi_E - \phi_P}{\Delta x^1}$, and the cross diffusion term $\frac{\phi_{te} - \phi_{be}}{\Delta x^2}$ and $\frac{\phi_{ne} - \phi_{se}}{\Delta x^3}$. We can find $\alpha_1, \alpha_2, \alpha_3$ by the procedure outlined above and finally compute the diffusion flux by

$$F_e^d = -\Gamma_\phi (\alpha_1 \frac{\phi_E - \phi_P}{\Delta x^1} + \alpha_2 \frac{\phi_{se} - \phi_{ne}}{\Delta x^2} + \alpha_3 \frac{\phi_{te} - \phi_{be}}{\Delta x^3}) \quad (2.35)$$

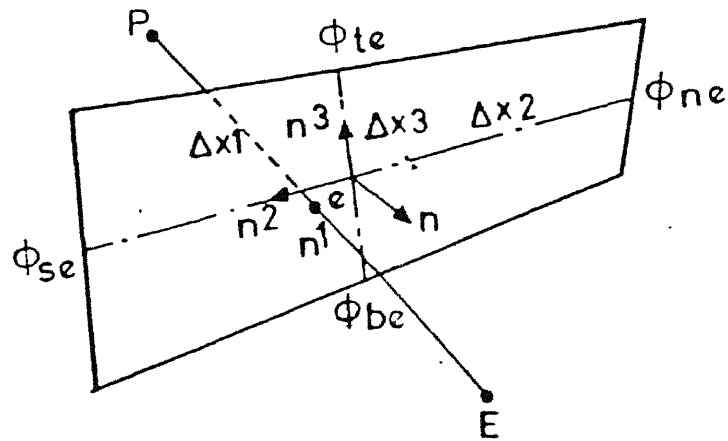


Figure 2.2: Face Representation

To calculate the edge center values appearing in cross-derivative diffusion flux the following interpolation scheme is proposed.

$$\phi_{te} = \frac{V_{TE}}{V_{tot}} \phi_P + \frac{V_P}{V_{tot}} \phi_{T,E} + \frac{V_T}{V_{tot}} \phi_E + \frac{V_E}{V_{tot}} \phi_T \quad (2.36)$$

$$\begin{aligned} V_{tot} &= V_{TE} + V_P + V_T + V_E \\ \phi_{be} = \frac{V_{BE}}{V_{tot}} \phi_P &+ \frac{V_P}{V_{tot}} \phi_{BE} + \frac{V_B}{V_{tot}} \phi_E + \frac{V_E}{V_{tot}} \phi_B \end{aligned} \quad (2.37)$$

$$\begin{aligned} V_{tot} &= V_{BE} + V_P + V_B + V_E \\ \phi_{ne} = \frac{V_{NE}}{V_{tot}} \phi_P &+ \frac{V_P}{V_{tot}} \phi_{NE} + \frac{V_N}{V_{tot}} \phi_E + \frac{V_E}{V_{tot}} \phi_N \end{aligned} \quad (2.38)$$

$$\begin{aligned} V_{tot} &= V_{NE} + V_P + V_N + V_E \\ \phi_{se} = \frac{V_{SE}}{V_{tot}} \phi_P &+ \frac{V_P}{V_{tot}} \phi_{SE} + \frac{V_S}{V_{tot}} \phi_E + \frac{V_E}{V_{tot}} \phi_S \\ V_{tot} &= V_{SE} + V_P + V_S + V_E \end{aligned} \quad (2.39)$$

where V_{TE} is the volume of the cell to the top-east of cell P etc. Other edge centers can be similarly interpolated.

(d) Sources

The source term is to be integrated over the cell volume. By assuming that the specific source at the CV center represents the mean value over the whole control volume, we can write

$$\int_V S_\phi dV \approx (S_\phi)_P V \quad (2.40)$$

Apart from the real source S_ϕ , explicitly treated parts of the convection and diffusion fluxes may also be added to S_ϕ . The momentum equation contain an extra term (pressure). This term is also treated explicitly. Its discretization is analogous to that of the ordinary diffusion flux. i.e., for the i^{th} momentum equation the pressure term is

$$-\int_S p n_i \mathbf{S} \approx -\sum_j p_j S_{ij}$$

where p_j is the pressure at the j^{th} face center and S_{ij} is the i^{th} component of the surface vector for face j .

2.4 Semi-Explicit Method

Existing methods which solve the incompressible Navier-Stokes equations fall into two categories, namely, semi-explicit and implicit schemes. In the first, the momentum equations are discretized in an explicit manner with the exception of the pressure gradient terms, which are treated implicitly; the continuity equation is also enforced implicitly. As a consequence, the equation-coupling reduces to a Poisson equation for the pressure corrections. Such schemes, however, because of their reliance on explicit differences, suffer from time-step restrictions. In the second category, the equations are discretized fully implicitly, with the coupling being more complicated. Some methods which fall within this group employ sequential iteration (such as the SIMPLE method and SIMPLER), in which the equations for each variable are solved repeatedly in succession.

2.4.1 Semi-Explicit Time-Stepping

For the present situation we will adopt semi-implicit scheme in which the equation

$$\rho V \frac{u_P^{n+1} - u_P^n}{\Delta t} + \sum_j (F^c + F^d)^n = - \sum_j p_j^{n+1} S_{ij} \quad (2.41)$$

has to be solved along with

$$\sum_j F_j^{n+1} = 0 \quad (2.42)$$

for each finite volume cell. We adopt a two step process. First a predicted velocity u^* is found which satisfies the equation

$$\rho V \frac{u_P^* - u_P^n}{\Delta t} + \sum_j (F^c + F^d)^n = - \sum_j p_j^n S_{ij} \quad (2.43)$$

Subtracting equation (2.43) from (2.41) we get

$$\rho V \frac{u'_P}{\Delta t} = - \sum_j p'_j S_{ij} \quad (2.44)$$

where the corrections

$$u'_P = u_P^{n+1} - u_P^n \quad p'_j = p_j^{n+1} - p_j^n \quad (2.45)$$

and the corresponding flux corrections F'_j have to satisfy

$$\sum_j F'_j = - \sum_j F_j^* \quad (2.46)$$

2.5 Pressure - Velocity Corrections

(Pressure Correction Poisson Equation)

Due to the non-staggered variable arrangement, if the variables (velocities and pressure) at the cell faces are calculated by linear interpolation between the adjacent cell centered quantities then the pressure-velocity iterations do not converge and lead to a *checker board* pressure field. Therefore it is important to use *momentum interpolation*[6] in which the velocity at the cell faces are computed by allowing linear interpolation of the convective and diffusive terms but not of the pressure term. This is done in the following way:

If the discretized equation for velocity is written as

$$\mathbf{u}_P = \mathbf{u}_P^{old} - \frac{\Delta t}{\rho V_P} (F_P^c + F_P^d) + \frac{\Delta t}{\rho V_P} S_u \quad (2.47)$$

where \mathbf{u}_P^{old} is the n^{th} time-step velocity and S_u is the pressure term. We define a new variable \mathbf{v}_P which is

$$\mathbf{v}_P = \mathbf{u}_P^{old} - \frac{\Delta t}{\rho V_P} (F_P^c + F_P^d) \quad (2.48)$$

Now to estimate the mass flux $F_e = \rho \mathbf{u}_e \cdot \mathbf{S}_e$ at the east face, straight forward linear interpolation would use.

$$F_e = \rho \overline{(\mathbf{u}_P, \mathbf{u}_E)} \cdot \mathbf{S}_e \quad (2.49)$$

where the over bar indicates a linear interpolation using equation (2.18). But momentum interpolation would use

$$F_e = \rho \overline{(\mathbf{v}_P, \mathbf{v}_E)} \cdot \mathbf{S}_e - \Delta t \nabla p \cdot \mathbf{S}_e \quad (2.50)$$

where the gradient ∇p is estimated using p_P, p_E and also other neighbours for a non-orthogonal grid.

The velocity and pressure fields are calculated with the following Gauss-Seidel type algorithm:

1. Use equation (2.47) to compute the cell-center \mathbf{u}_P and \mathbf{v}_P . Make an initial guess p_P . Use interpolation (Eq. 2.18) to obtain the face-center quantities \mathbf{v}_j and p_j .
2. Compute the mass flux through each cell face j using

$$F_j^* = \rho \mathbf{v}_j \cdot \mathbf{S}_j - \Delta t \nabla p_j \cdot \mathbf{S}_j \quad (2.51)$$

3. Use equation $\mathbf{u}'_j = -\frac{\Delta t}{\rho} \nabla p'_j$ to compute the flux correction at the face j ,

$$F'_j = -\Delta t \nabla p'_j \cdot \mathbf{S}_j \quad (2.52)$$

This is computed using the formulation for diffusion fluxes [equations (2.28-2.35)] replacing ϕ by p' .

4. Compute residual for each cell.

$$\mathfrak{R} = - \sum_j F_j^* - \sum_j F'_j \quad (2.53)$$

5. Calculate the cell-center pressure correction from the relation

$$p'_P = p'_P + \omega \frac{\mathfrak{R}}{a_P} \quad (2.54)$$

where ω is relaxation factor and a_P stands for diagonal coefficients that is calculated from

$$a_P = -\Delta t \left[\frac{\alpha_1}{\Delta x^1} |_w - \frac{\alpha_1}{\Delta x^1} |_e + \frac{\alpha_2}{\Delta x^2} |_n - \frac{\alpha_2}{\Delta x^2} |_s + \frac{\alpha_3}{\Delta x^3} |_b - \frac{\alpha_3}{\Delta x^3} |_t \right] \quad (2.55)$$

where α_1, α_2 , etc. are the same as in equations (2.28-2.35).

6. If $\mathfrak{R}_{rms} > \epsilon$ goto step 3

7. Store the updated mass flux through cell-faces from

$$F_j^* = F_j^* - \Delta t \nabla p'_j \cdot \mathbf{S}_j \quad (2.56)$$

8. Store the updated pressure at cell-center $p_P = p_P + p'_P$

9. Store the cell-center corrected velocity

$$\mathbf{u}'_P = -\frac{\Delta t}{\rho V_P} \sum_j p'_j S_{ij}. \quad (2.57)$$

$$\mathbf{u}_P = \mathbf{u}_P + \mathbf{u}'_P \quad (2.58)$$

10. Goto step 1 and repeat the process until steady state is reached.

It can be shown that satisfying equation (2.46) is the same as solving

$$\nabla^2 p' = -\frac{\nabla \cdot \mathbf{u}^*}{\Delta t} \quad (2.59)$$

and finding the corrections

$$\mathbf{u}' = -\Delta t \nabla p' \quad (2.60)$$

such that

$$\mathbf{u}^{n+1} = \mathbf{u}^* + \mathbf{u}' \quad (2.61)$$

$$p^{n+1} = p^n + p' \quad (2.62)$$

Thus the procedure above can be called the **pressure correction Poisson solver**.

It should be noted that in this code we compute a pseudo pressure field which allows us to satisfy the continuity equation. The pseudo pressure (or pressure correction approach) allows us to use simple boundary conditions for pressure.

2.6 Initial and Boundary Conditions

The following boundary conditions can be incorporated:

- No-slip boundary conditions

$$\mathbf{u} = 0$$

- Specified boundary conditions

$$\mathbf{u} = \mathbf{u}_0$$

- Free-slip boundary conditions

$$\mathbf{u}_n = 0, \quad \frac{\partial \mathbf{u}_t}{\partial n} = 0$$

where n represents the normal to the boundary. The boundary conditions for the pressure correction are

$$\text{For pressure correction } \frac{\partial p'}{\partial n} = 0$$

The boundary conditions for velocity and pressure correction are implemented easily using fictitious cells.

Chapter 3

Results and Discussion

3.1 Flow In Curved Ducts

Flows in curved ducts occur in diverse applications such as centrifugal pumps, aircraft intakes, river bends and in the cooling coils of heat exchangers. A characteristic which distinguishes such flows from those in straight ducts is (a) the generation of stream wise vorticity or "secondary motion" within the duct, resulting in a pressure loss, (b) the spatial redistribution of stream wise velocity and (c) increased heat transfer at the duct walls. The nature of the secondary flow depends, among other parameters, on the curvature ratio of the pipe $\delta=R/d$ (where R is the mean radius of curvature of the bend and d is the hydraulic diameter of the duct) and the flow Reynolds number.

The present work consists of numerical experiments on 90° and 180° bends of square and circular cross section with strong curvature. For the problems considered the steady state solution is obtained by the false-transient approach, *i.e.*, by time marching the unsteady governing equations. The unsteady Navier-Stokes equations describing the flow are :

$$\frac{\partial u}{\partial x} + \frac{\partial v}{\partial y} + \frac{\partial w}{\partial z} = 0 \quad (3.1)$$

$$\frac{\partial u}{\partial t} + \frac{\partial u^2}{\partial x} + \frac{\partial uv}{\partial y} + \frac{\partial uw}{\partial z} = -\frac{\partial p}{\partial x} - \frac{1}{Re} \nabla^2 u \quad (3.2)$$

$$\frac{\partial v}{\partial t} + \frac{\partial vu}{\partial x} + \frac{\partial v^2}{\partial y} + \frac{\partial vw}{\partial z} = -\frac{\partial p}{\partial y} + \frac{1}{Re} \nabla^2 v \quad (3.3)$$

$$\frac{\partial w}{\partial t} + \frac{\partial uw}{\partial x} + \frac{\partial vw}{\partial y} + \frac{\partial w^2}{\partial z} = -\frac{\partial p}{\partial z} + \frac{1}{Re} \nabla^2 w \quad (3.4)$$

In the above equations, the velocities have been nondimensionalized with respect to the inlet velocity U , and all lengths have been nondimensionalized with respect to the hydraulic diameter d . The Reynolds number, is given by $Re = \frac{V_c d}{\nu}$ where V_c is the bulk mean velocity and ν is the kinematic viscosity of the fluid.

3.2 Flow In A 90° Bend Square Curved Duct

3.2.1 Problem Description

The problem geometry is shown in isometric view in the figure 3.1 . It consists of a 90° bend of unit square cross section with a mean radius of curvature of $R=2.3$ and with straight extensions upstream and downstream of lengths that are 45 times the hydraulic diameter.

The flow parameters for this case are Re of 790, based on inflow conditions and the hydraulic diameter d ($\equiv 4.0 \times \text{Area}/\text{Perimeter}$) of the duct, curvature ratio $\delta=2.3$ ($\equiv R/d$) where R is the mean radius of curvature of the bend duct. The computational domain consists of 64 stations in the stream wise direction (with 30 stations in the bend) and a 24X24 grid in the cross plane.

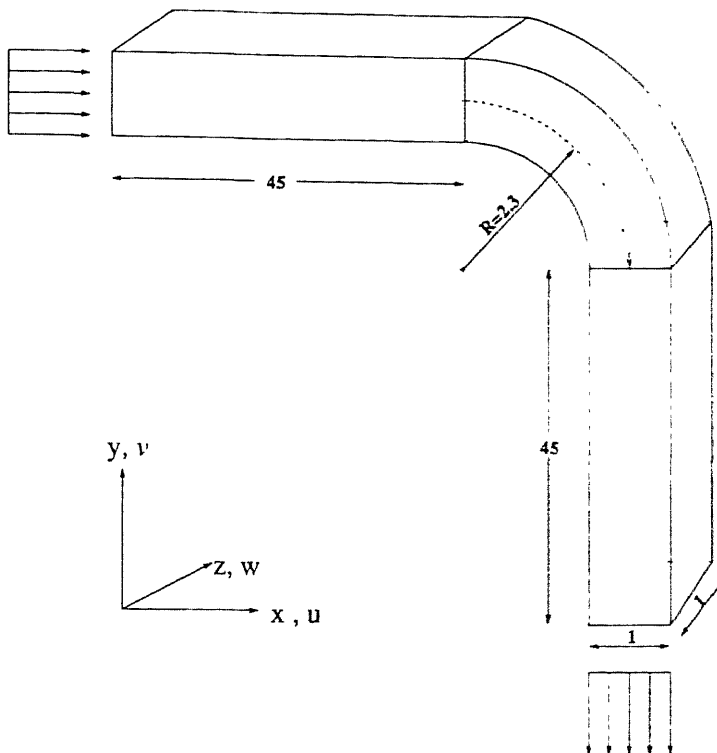


Figure 3.1: Schematic of 90° bend square duct

The initial conditions, which are arbitrary for this steady state problem, are zero velocity conditions. The boundary conditions for the problem are given by no slip conditions on the walls and

$$\begin{aligned} u &= 1, v = w = 0 \quad \text{at} \quad \text{inlet} \\ u &= \frac{\partial v}{\partial y} = w = 0 \quad \text{at} \quad \text{outlet}. \end{aligned}$$

3.2.2 Results

In the bend the fluid moves away from the inner radius wall towards the outer radius wall under the influence of centrifugal forces. The velocity vector profiles in the x - y plane (the plane of symmetry) depicted in the figure 3.2 show this

phenomenon. The profile is parabolic at the entry of the bend and we can observe between 30° and 90° stations a large deceleration in the flow at the inner radius and a corresponding acceleration at the outer radius wall.

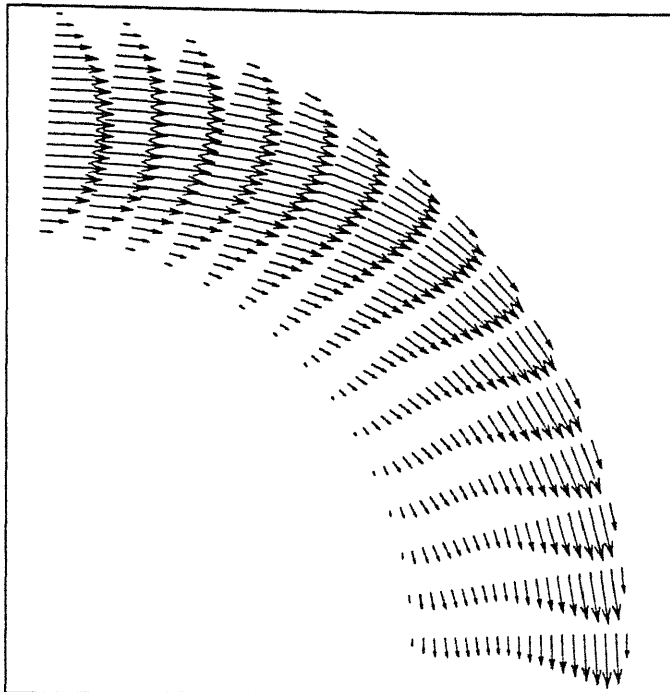


Figure 3.2: Velocity vectors in the symmetry plane of a 90° bend duct

The structure of the streamwise velocity is shown in the contours of constant azimuthal velocity (U_ϕ) in the figures 3.3 and 3.4. The figures demonstrate the complexity of the flow. The velocity contours show that with the progressive movement, the high velocity region is found nearer to the outer wall and along the side walls with a corresponding low velocity region adjacent to the inner wall. This problem has been solved for the same configuration and the same parameter set, as the experiment of Humphrey et al.[10], who also numerically simulated their experiment. The figure 3.5 shows the present results in comparison with the experimental and computed data of ref[10].

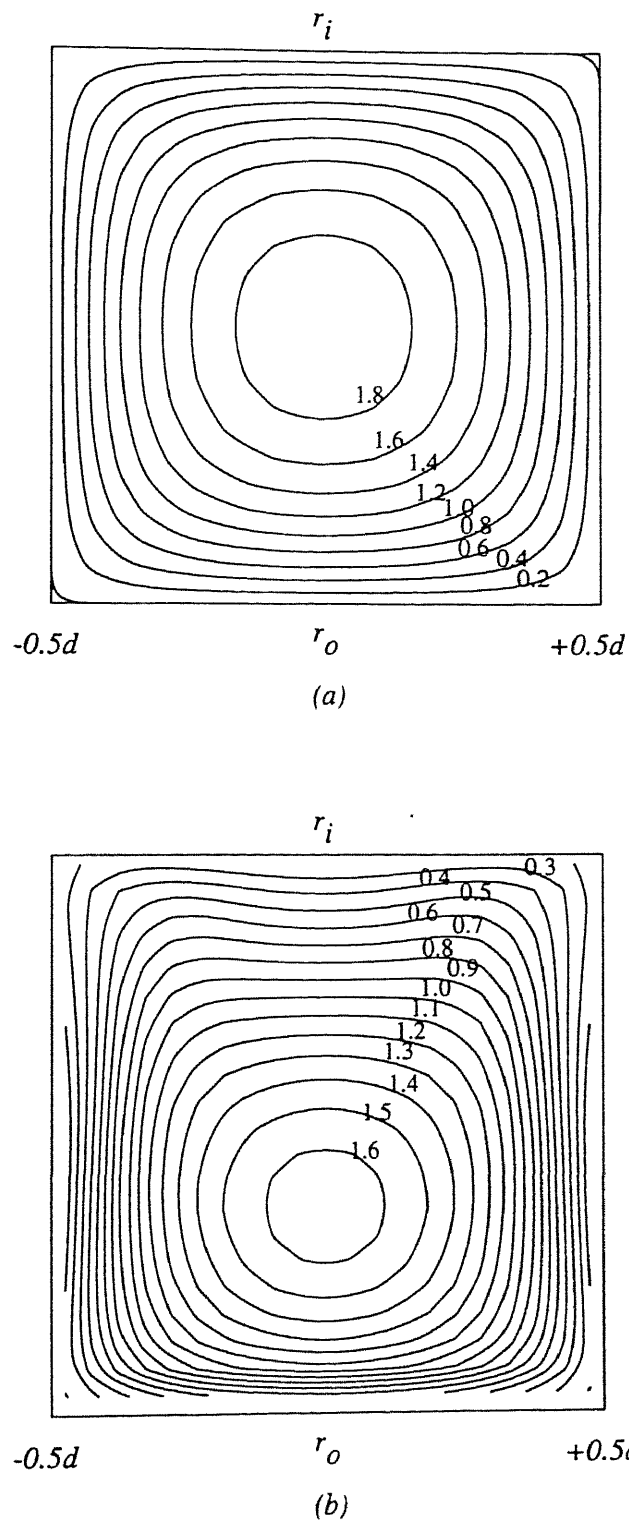
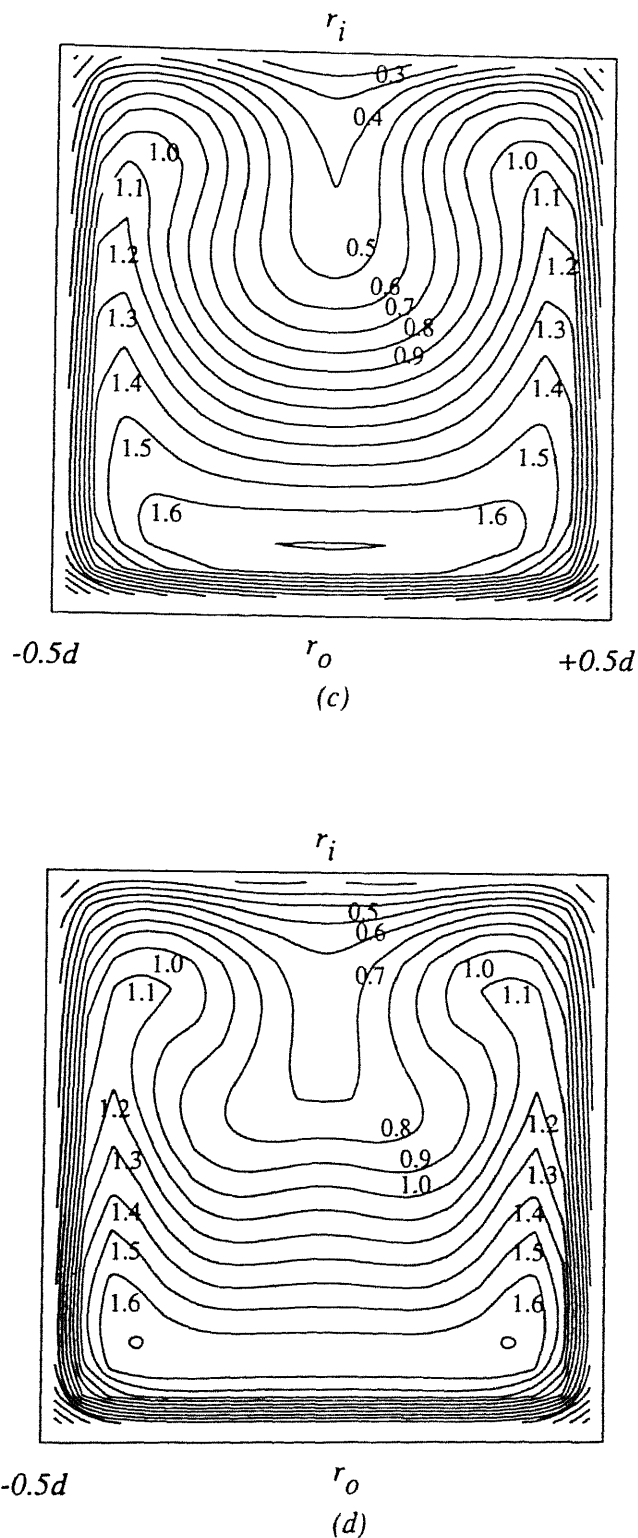


Figure 3.3: Velocity contours in the 90^0 bend flow at (a) $\phi=0^0$, (b) $\phi=30^0$

Figure 3.4: Velocity contours in the 90^0 bend flow at (c) $\phi=60^0$, (d) $\phi=90^0$

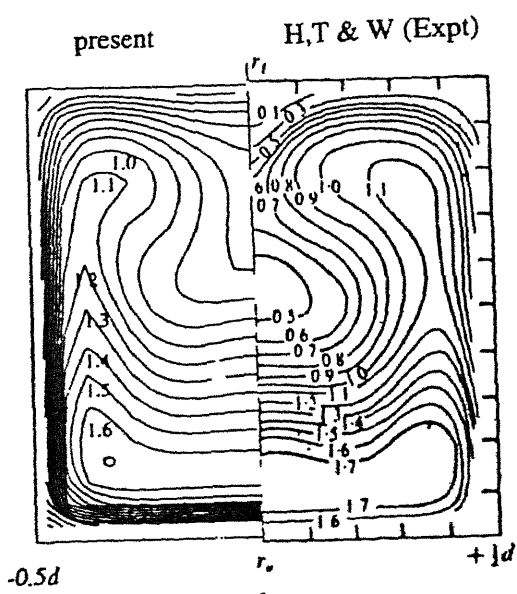
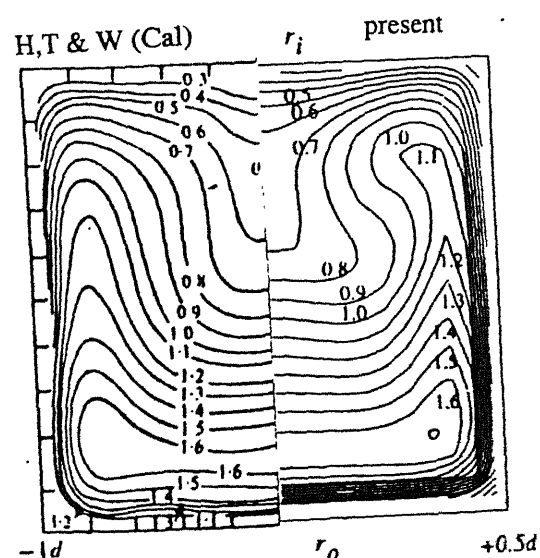
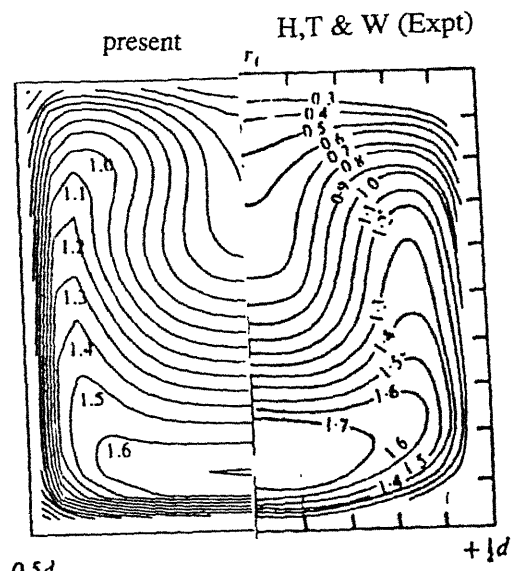
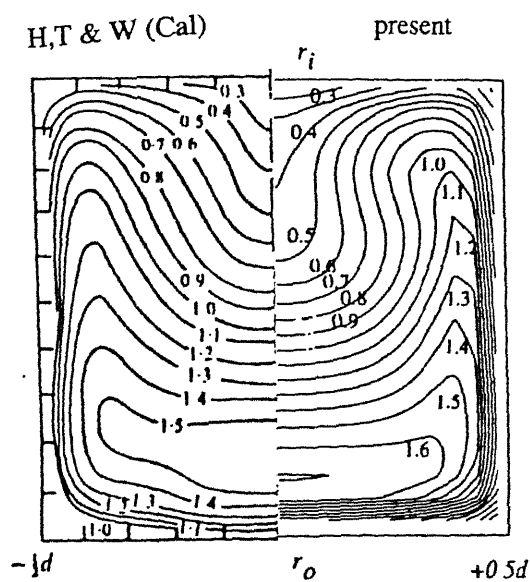
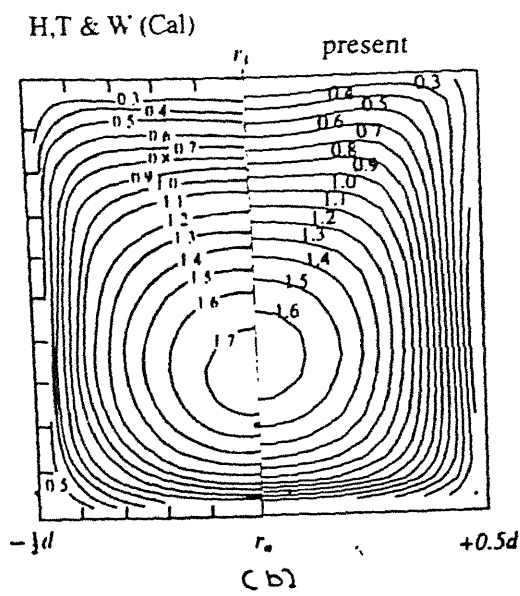
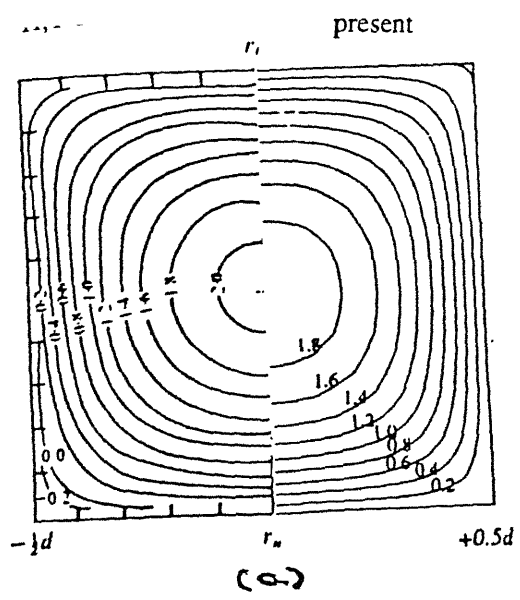
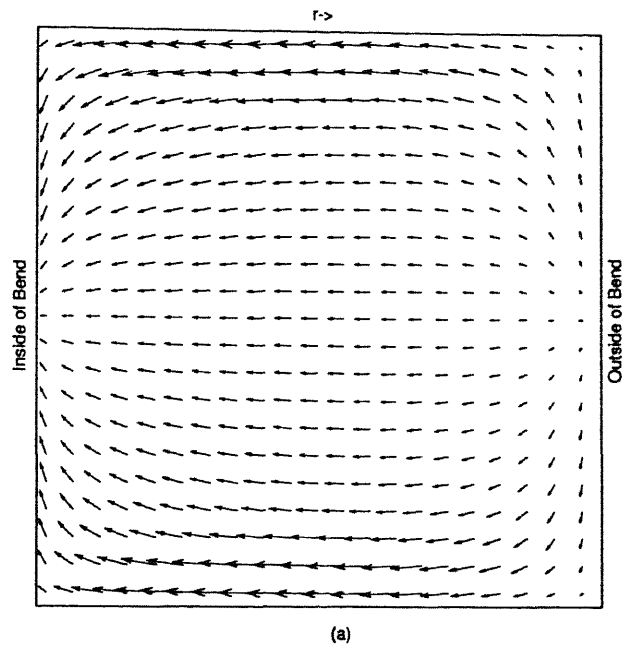
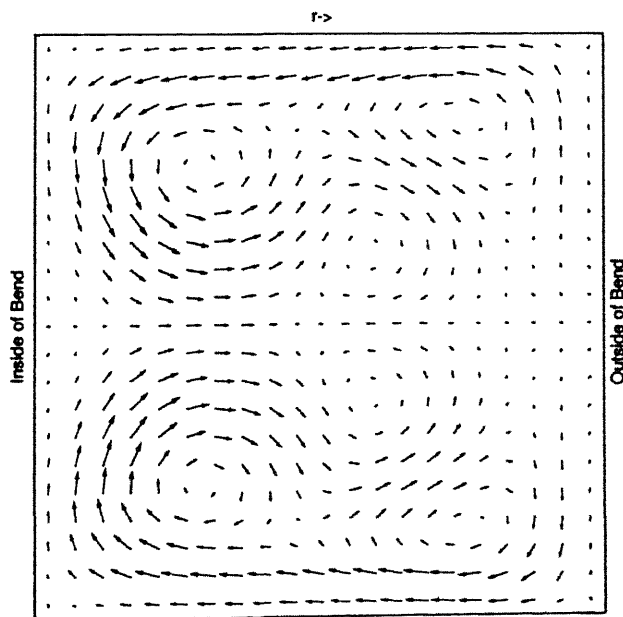


Figure 3.5: The present results in comparison with ref[10] (a) 0° , (b) 30° , (c) 60° , (d) 90° .

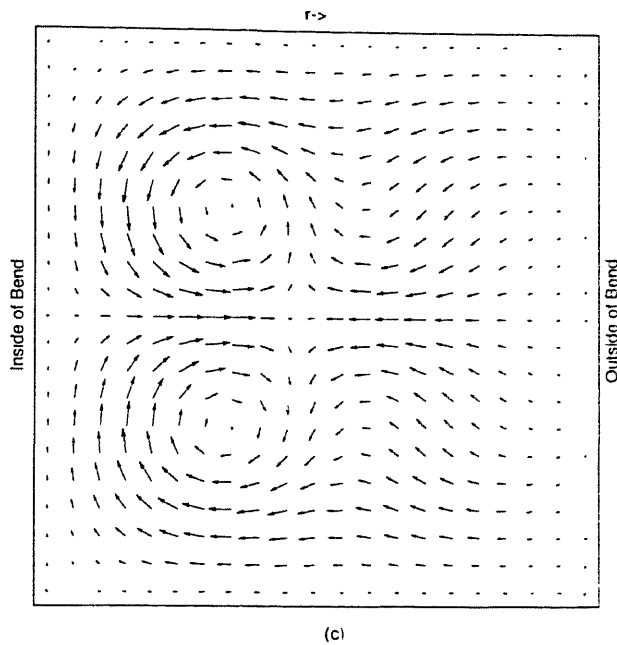


(a)

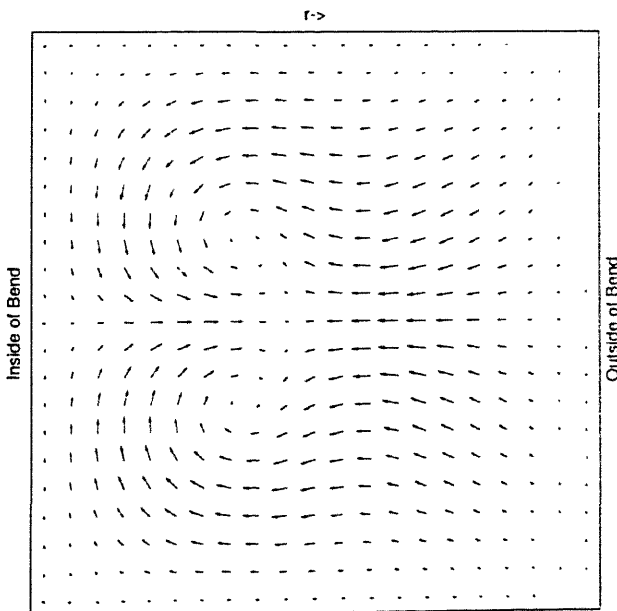


(b)

Figure 3.6: Vector plots of secondary velocity at (a) $\phi=0^0$, (b) $\phi=90^0$



(c)



(d)

Figure 3.7: Vector plots of secondary velocity at : (c) 9.0 d. (d) 15.75 d

The secondary flow in the bend is shown at different locations by the cross flow velocity vectors in the figures 3.6 and 3.7. Figures (a) and (b) show the cross sectional flow at $\phi=0^{\circ}$ and 90° respectively, while (c) and (d) show the same at distances 9 d and 15.75 d downstream of (the 90° point of) the bend. It can be seen that the secondary flow is quite complex and that it persists for some distance downstream of the bend.

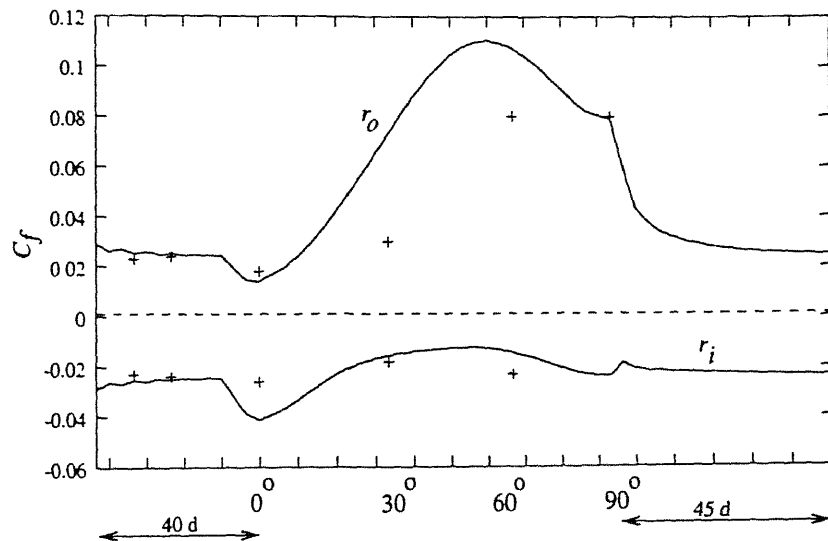


Figure 3.8: Measured(+) and computed friction coefficients at the center-line of the inside and outside curved walls of the bend.

The figure 3.8 shows the computed friction coefficients comparing with the measured results by Ward-Smith(1971). The coefficients at the outer and inner duct walls are plotted as positive and negative on the figure 3.8, merely to distinguish between them. While the initial magnitudes are the same, the C_f at the outer wall increases dramatically in the bend and does not regain fully-developed values till some distance downstream. The C_f at the inner wall does not show such marked variation. The differences arise due to the secondary flow structure seen in the previous figures.

3.3 Flow In A 180^0 Bend Square Curved Duct

3.3.1 Problem Description

The problem considered is the same in configuration and parameters as the experimental work of Phille et al.[14] and is shown in isometric view in figure 3.9. The model consists of a 180 degree bend of unit square cross section with a mean radius of curvature of $R=6.45$, and has straight extensions upstream and downstream that are 56 times the hydraulic diameter. The inlet section is sufficiently longer to ensure fully developed flow.

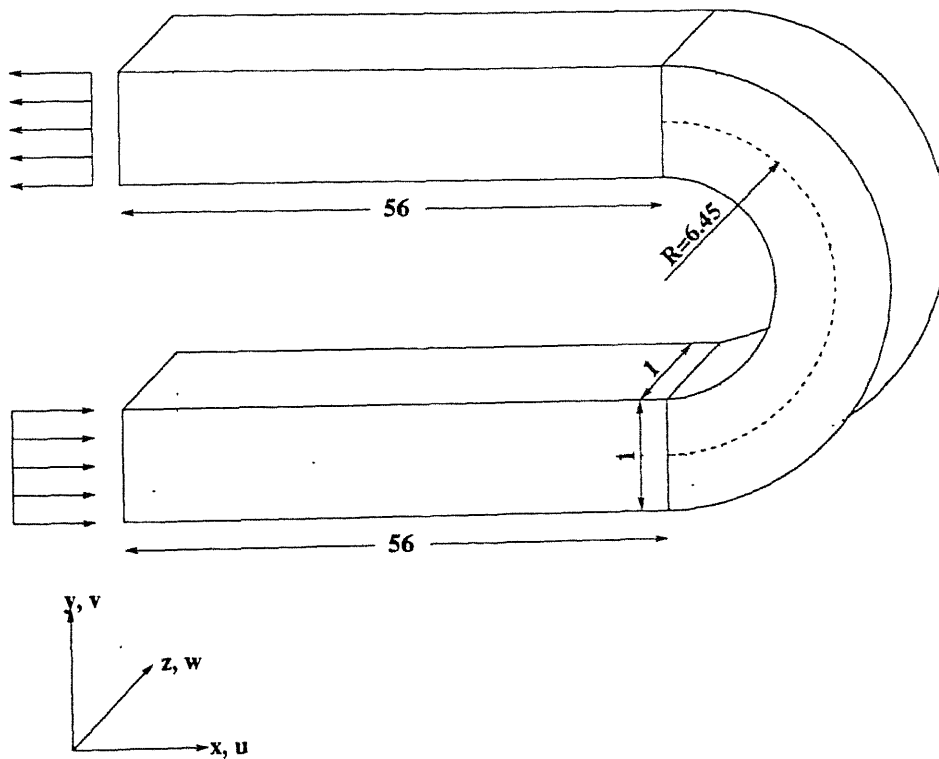


Figure 3.9: Schematic of 180^0 bend square duct

The flow parameters are Re of 574 ($Re = \frac{V_c d}{\nu}$), where V_c is the bulk mean velocity and ν is the kinematic viscosity of the fluid, and a curvature ratio $\delta (\equiv R/d) = 6.45$. This is a very severe test case where the flow is quite complex. The present computations are done on a relatively coarse grid with 60 stations in the bend and a (24X24) grid in the cross plane.

The initial conditions, which are arbitrary, for this steady state problem, are zero velocity conditions. The boundary conditions are no slip conditions at the walls and

$$\begin{aligned} u &= 1, v = w = 0 \quad \text{at} \quad \text{inlet} \\ \frac{\partial u}{\partial x} &= v = w = 0 \quad \text{at} \quad \text{outlet}. \end{aligned}$$

3.3.2 Results

Centrifugal forces arising due to the presence of longitudinal curvature causes the peak of the axial velocity profiles to shift towards the outer wall. The streamwise flow development is summarized in the figure 3.10.

The flow development in the bend is depicted in the figures 3.11 to 3.14 which show the azimuthal velocity component U_c measured as a function of radial coordinate in the mid plane of the cross section, $z=0.5$, at intervals of 18⁰. The figures show the comparison of the present results with the computed results of Kaushik and Rubin ref[13], obtained on the same sized grid and the experimental data[14]. The results are in close agreement with each other.

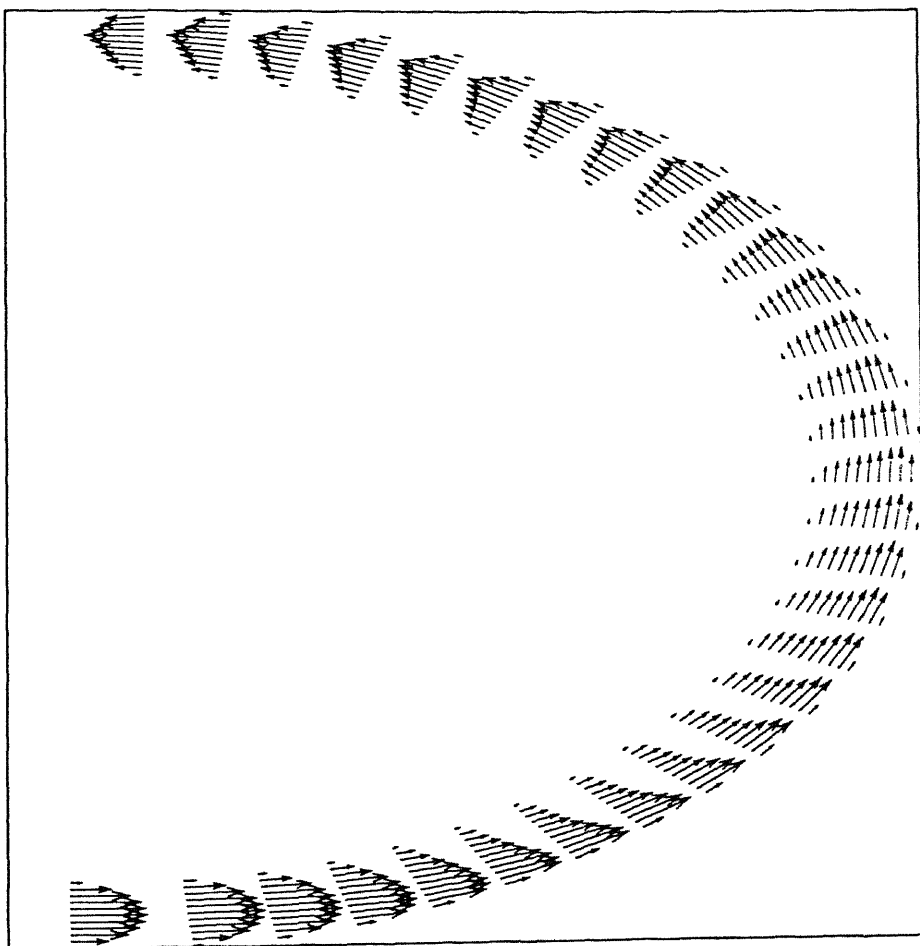


Figure 3.10: Streamwise velocity development in the bend shown as velocity vectors plotted in the x - y plane of symmetry.

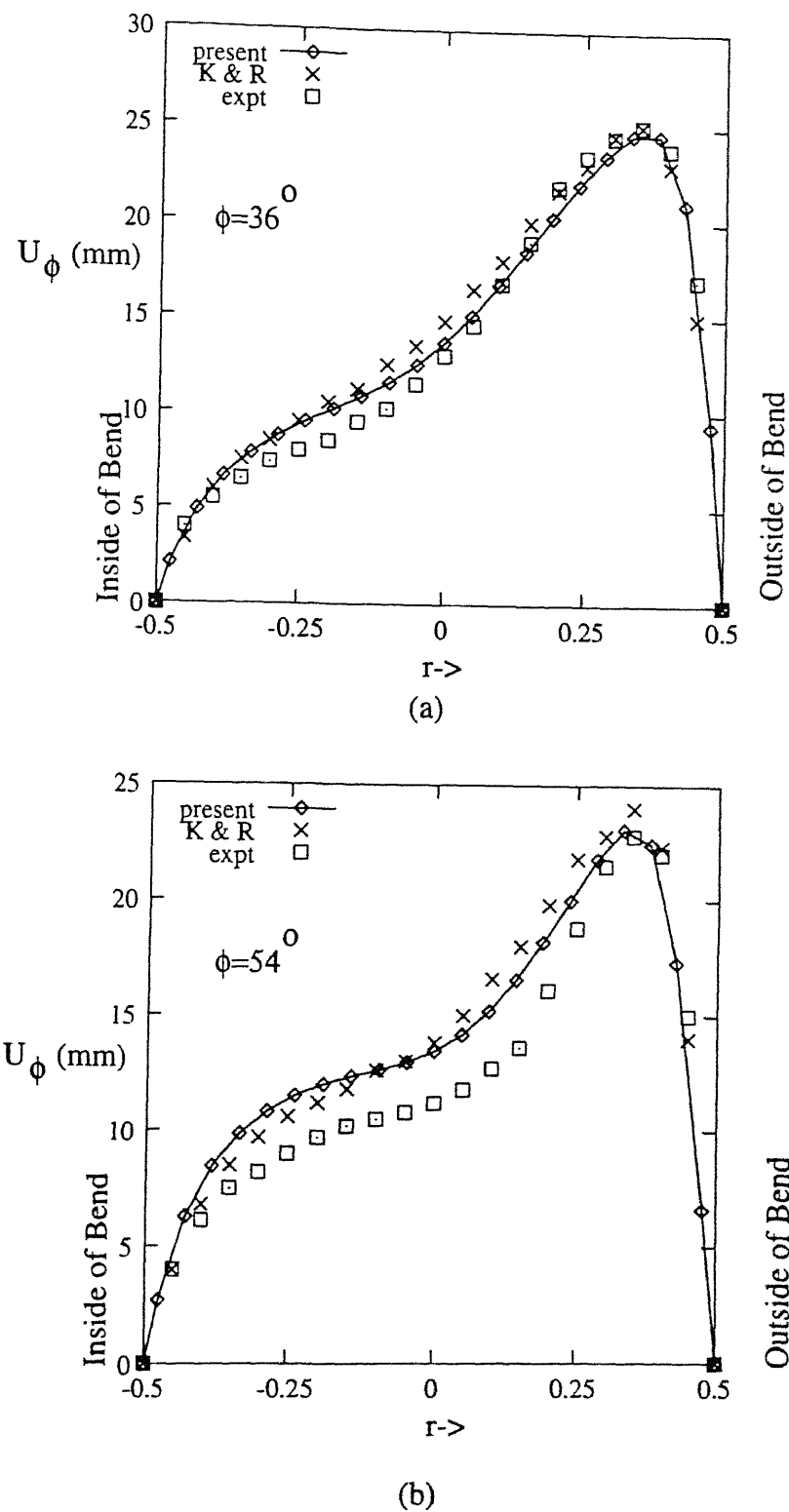
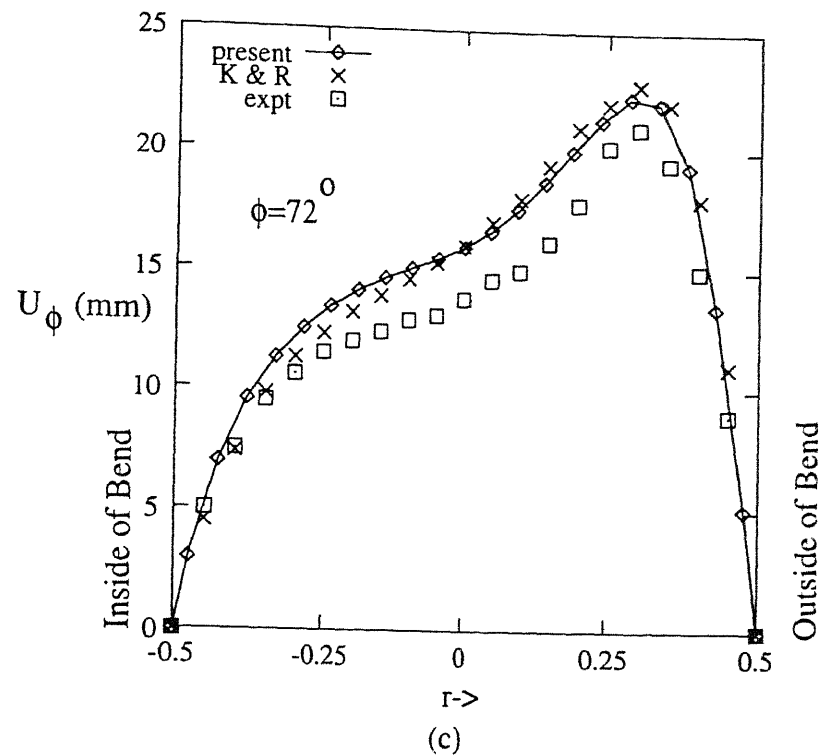
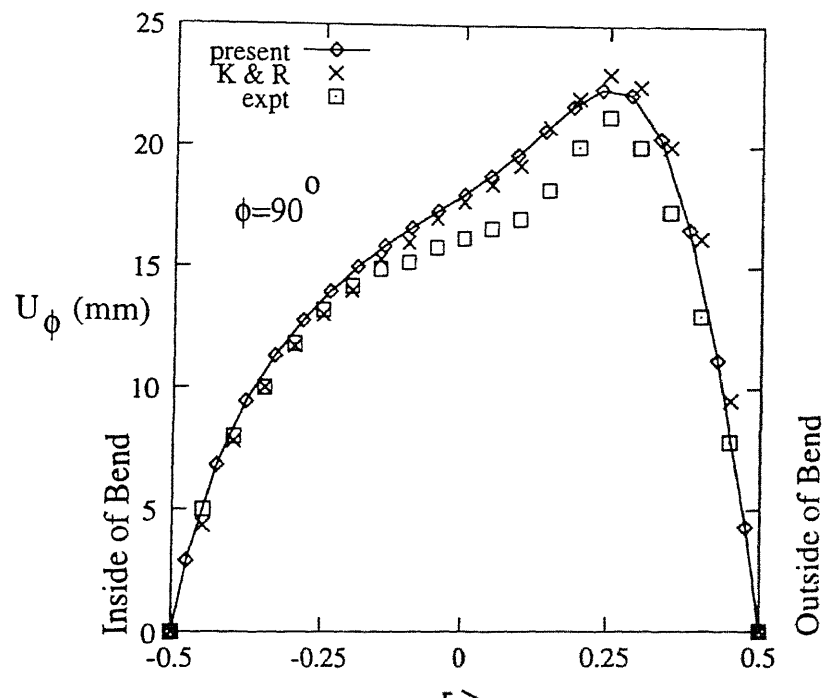


Figure 3.11: Mainstream velocity as a function of the radial location r at $z=0.5$
(a) $\phi=36^\circ$, (b) $\phi=54^\circ$



(c)



(d)

Figure 3.12: Mainstream velocity as a function of the radial location r at $z=0.5$
(c) $\phi=72^\circ$, (d) $\phi=90^\circ$

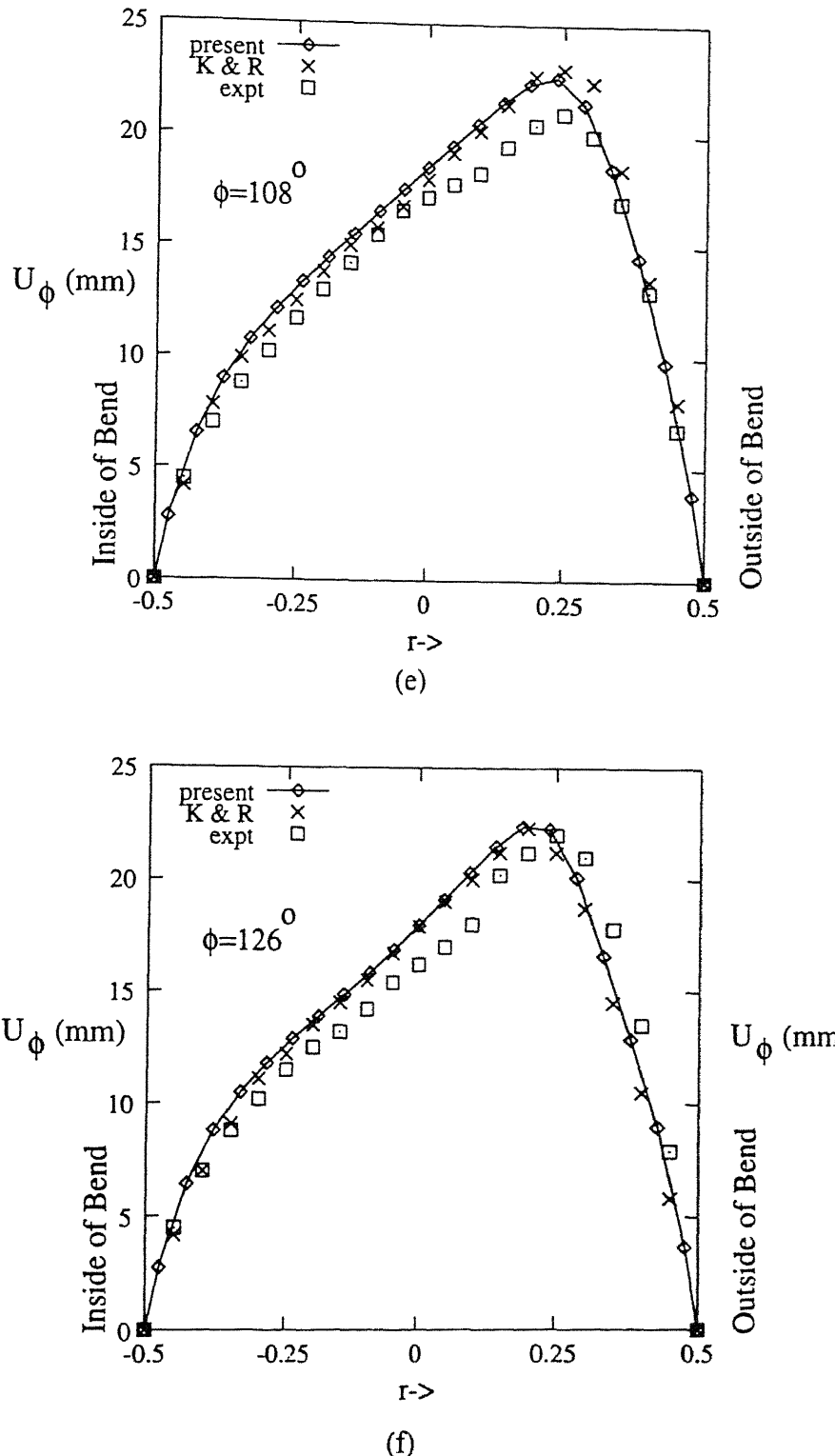


Figure 3.13: Mainstream velocity as a function of the radial location r at $z=0.5$
(e) $\phi=108^0$, (f) $\phi=126^0$

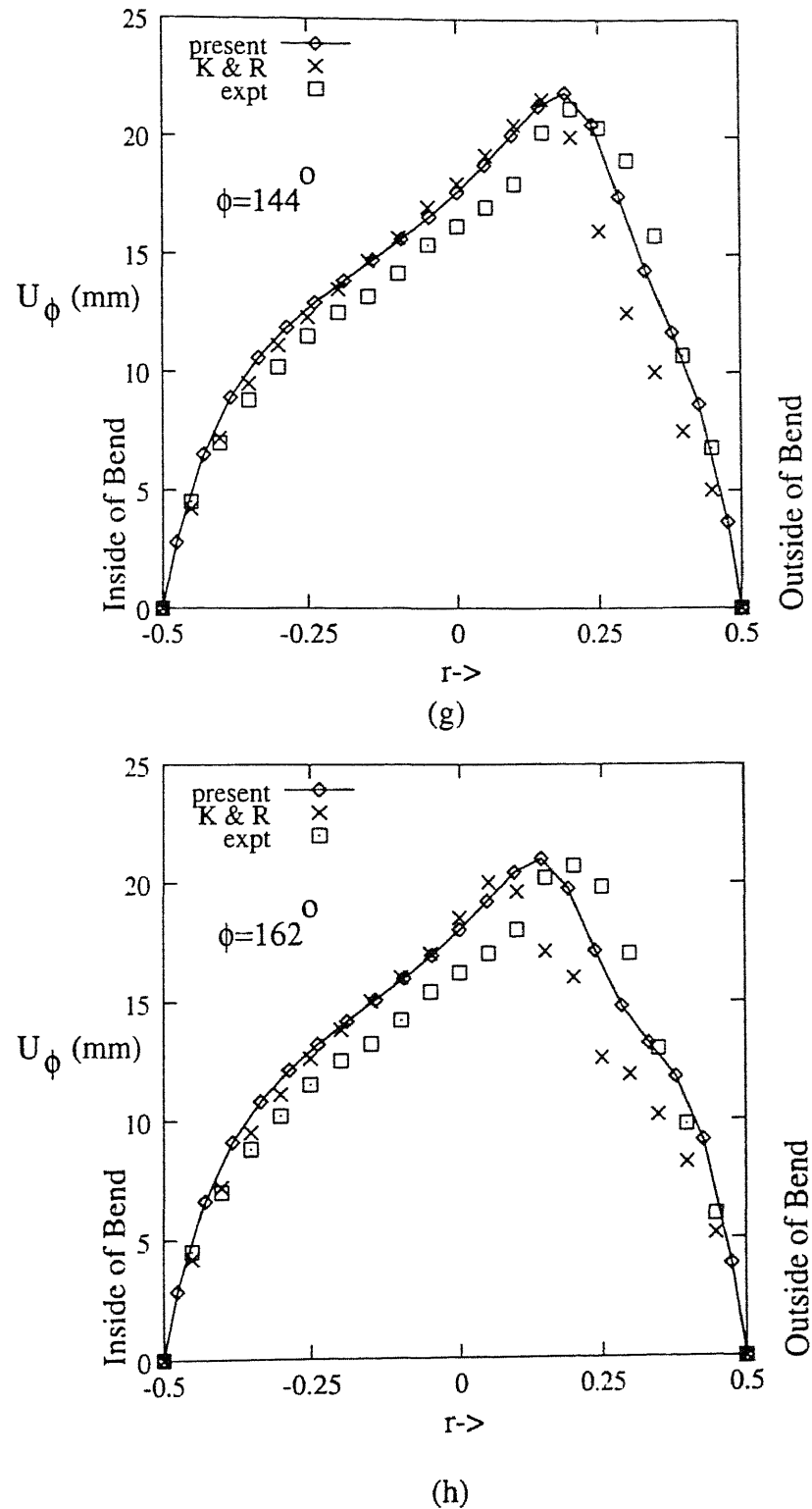


Figure 3.14: Mainstream velocity as a function of the radial location r at $z=0.5$
(g) $\phi=144^\circ$, (h) $\phi=162^\circ$

The figure 3.15 shows the presence of two pairs of counter rotating primary and secondary vortices. This is in agreement with the experimental data which shows the presence of a second vortex pair in the region between $\phi=108^0$ and 171^0 .

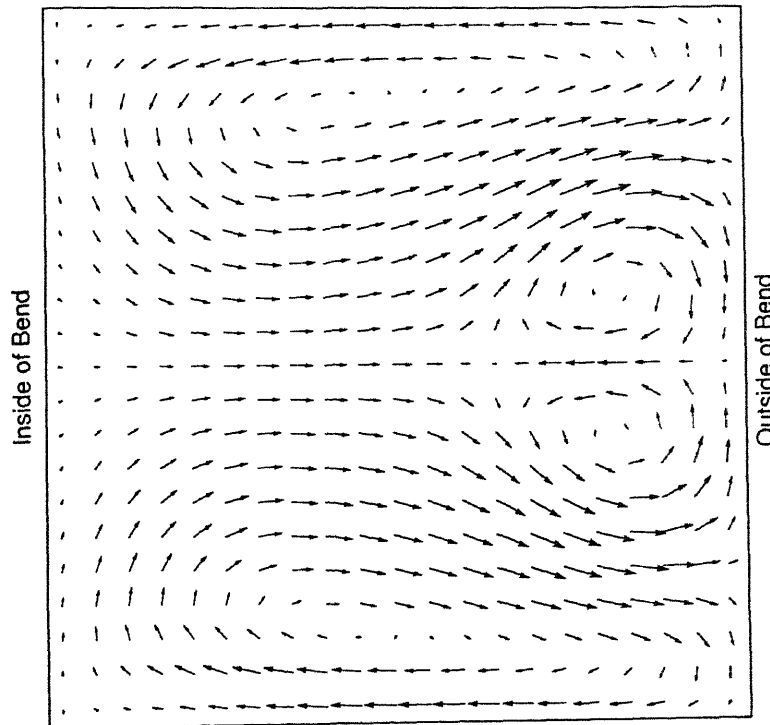


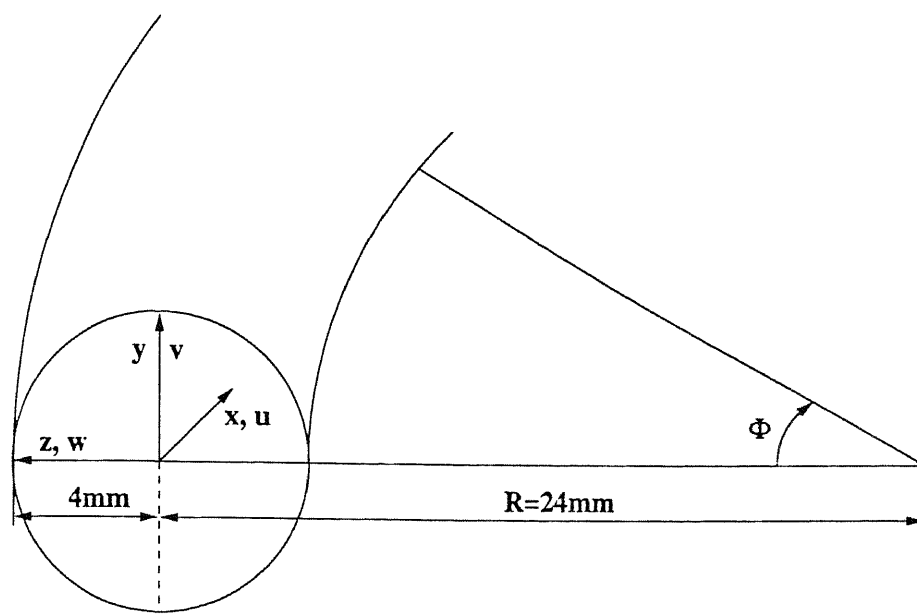
Figure 3.15: Two dimensional vector profiles of the secondary velocities at $\phi=162^0$.

3.4 Flow In A 90⁰ Bend Circular Duct

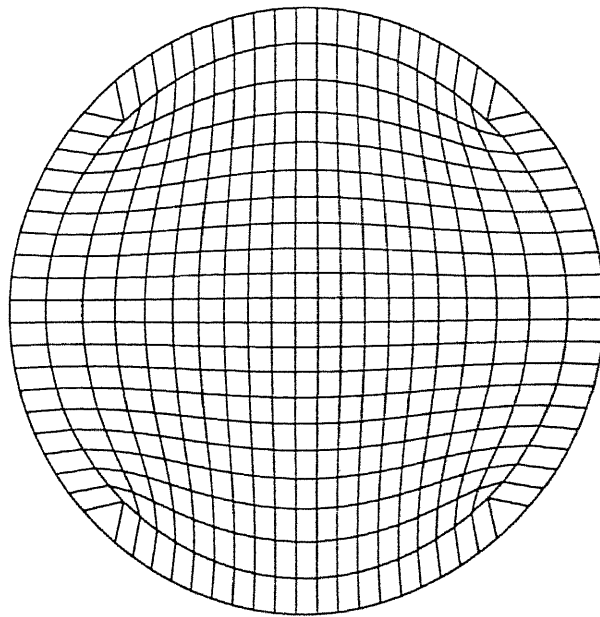
3.4.1 Problem Description

The flow in a 90⁰ bend of circular cross section is again a stringent test for a solver for flows in complex geometry. The problem considered is same as in the experimental work of Bovendeerd[15] and is shown in fig.3.16(a). The model consists of a 90⁰ bend in circular cross section pipe of diameter of 8mm and a bend of a mean radius of curvature 24mm. The model has a straight extension downstream that is 12.5 times the hydraulic diameter. A fully developed parabolic profile is introduced at the entrance of the bend (in the experimental[15] a long inlet section ensured near parabolic profile at the bend entrance).

The flow parameters are a Reynolds number $Re(Re = \frac{V_c d}{\nu}) = 700$ where V_c is the bulk mean velocity and ν is the kinematic viscosity of the fluid, and a curvature ratio $\delta(\equiv R/d)=3$. The grid employed for the circular cross section is shown in fig.3.16(b). The grid was generated using a Laplace method[16]. [First a circular grid with a diameter of 7.75mm was generated using Laplace method which mapped it onto a square. Another grid point was added on each side with a diameter of 8.25mm which ensured that the cell points on the outer control volumes were exactly at 8mm which represents the physical domain. However one cell point at every 45⁰ still could not fall on the physical domain as the control volume is not exactly orthogonal. For this case the boundary conditions are imposed on the cell points which represents the physical domain and hence no fictitious cells. The zero pressure conditions at the outlet which were implemented for the earlier problems created numerical problems and the results were obtained by implementing Neumann boundary conditions at the outlet]. The computational domain consists of 51 stations in the streamwise direction (with 30 stations in the bend) and a 22X22 grid in the cross plane.



(a)



(b)

Figure 3.16: (a) Co-Ordinates of the bend (b) Grid Implemented

The initial conditions for this steady state problem are positive and negative parabolic profiles for u and v respectively, and $w=0$. The boundary conditions are zero velocities at the cells on the cross section. a positive parabolic profile of u [with v and w being zero] at the inlet and a Neumann boundary condition for v [with u and w being zero] at the outlet.

3.4.2 Results

The velocity measurements are shown at seven axial stations in the bend corresponding to $\phi = 0^0, 4.5^0, 12^0, 22.5^0, 40.5^0, 58.5^0$ and 82.5^0 . [Some of the results were interpolated so as to have the results in near comparison to the experimental[15] whose axial stations in the bend were at $\phi=0^0, 4.6^0, 11.7^0, 23.4^0, 39.8^0, 58.5^0$ and 81.9^0]. The development of the axial flow in the plane of symmetry is shown in fig.3.17. The curvature has no effect on the velocity profiles between $\phi=0^0$ to 12^0 . Further downstream the maximum of the axial velocity(U_ϕ) has shifted towards the outer bend reflecting the strong curvature effects.

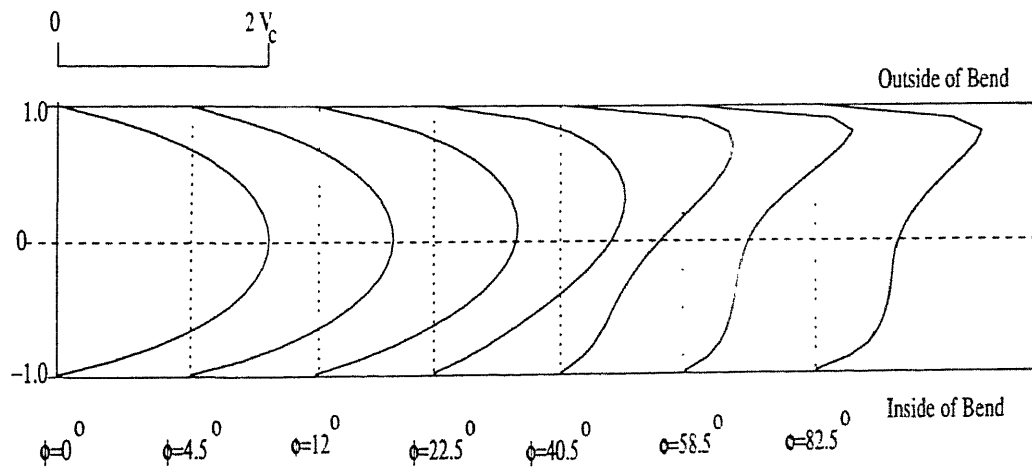
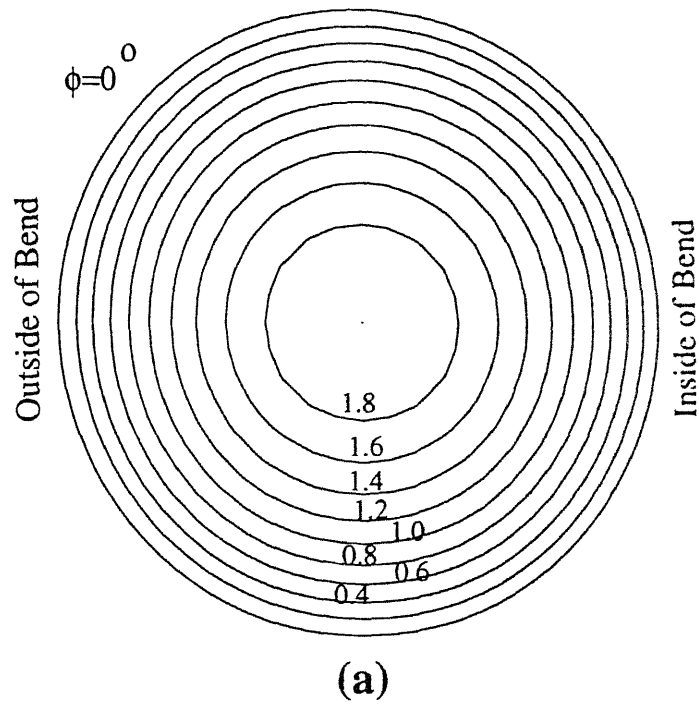


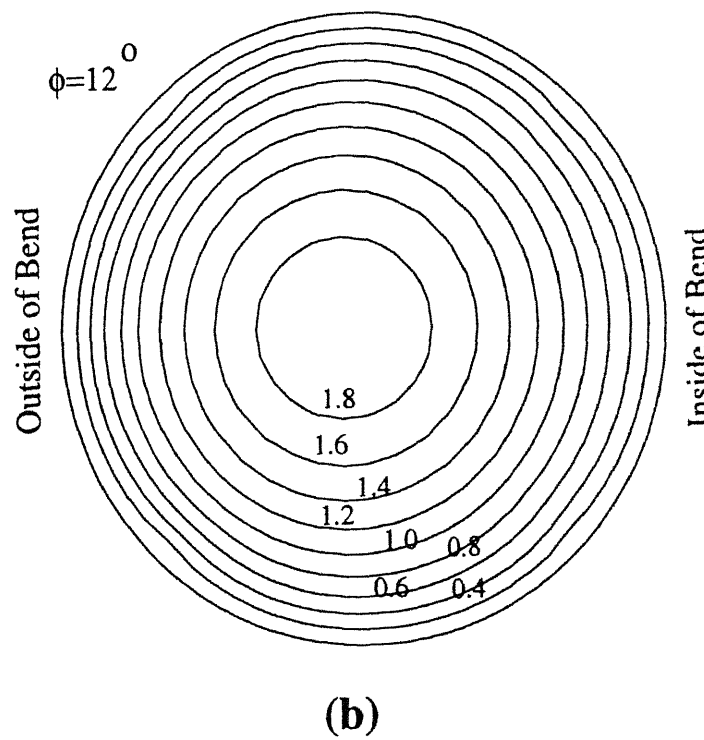
Figure 3.17: Development of the axial flow in the plane of symmetry

A clear picture of the axial flow is given in the figures 3.18 to 3.20 in which the axial velocity is represented by isovelocity contours. We can observe that at $\phi=22.5^0$ the contours have shifted towards the outer bend becoming elliptic in shape. Further downstream we can see that the minimum of axial velocity has shifted towards the outer wall, while a region of relatively low axial velocity has appeared near the inner wall. At $\phi=40.5^0$ the region of low axial velocity has expanded from the inner wall along the plane of symmetry towards the tube. At the last station $\phi=82.5^0$ near the inner wall the axial velocity has increased. The results are shown in comparison with the experimental[15] in the fig.3.21.

The secondary flow in the bend is shown in the fig.3.4.2 as velocity vectors in the cross plane. At $\phi=4.5^0$ the vector plot shows the incipience of a vortex pair which gets intensified further downstream. At $\phi=22.5^0$ the vortex has shifted outwards. At $\phi=58.5^0$ the higher secondary velocities appear at the inner half of the bend. At $\phi=82.5^0$ the vortex has developed a 'tail' towards the upper wall (as seen by[15]) and the secondary flow has sharply reduced but remains complex in structure. The figures are substantially similar in detail to the experimental data of [15].

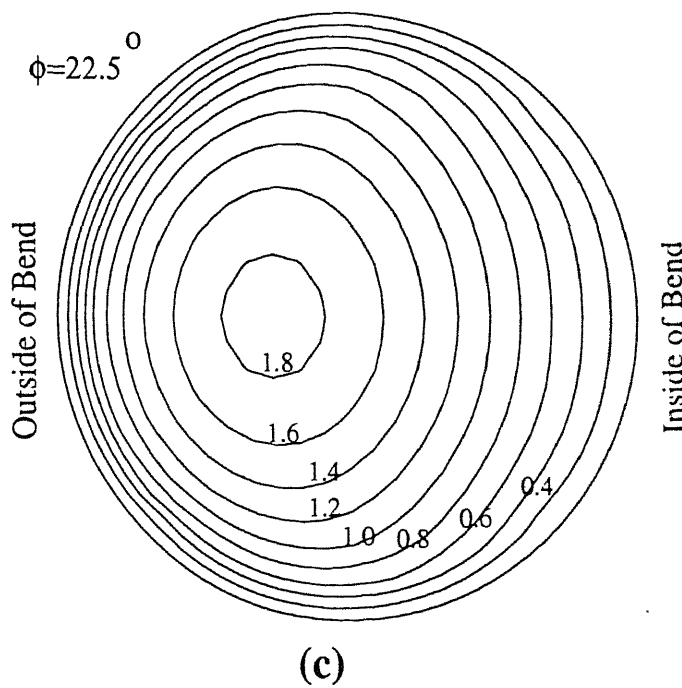


(a)

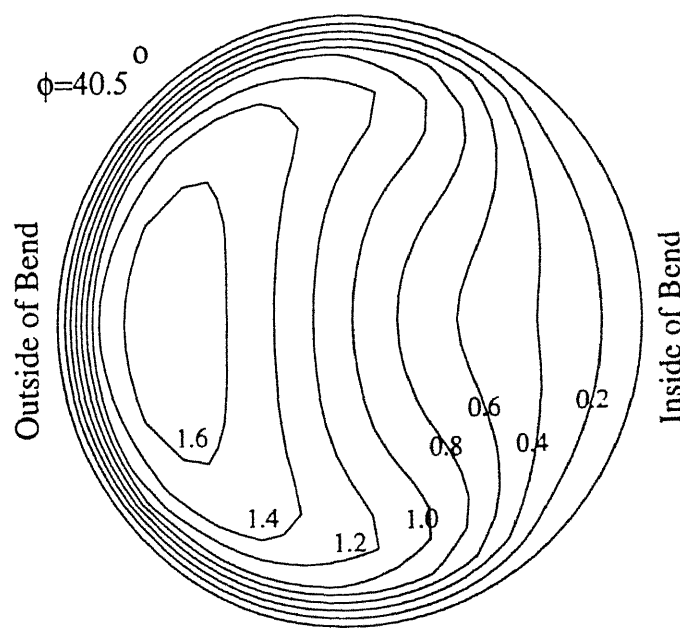


(b)

Figure 3.18: Development of the axial flow represented by isovelocity contours at (a) $\phi=0^{\circ}$, (b) $\phi=12^{\circ}$

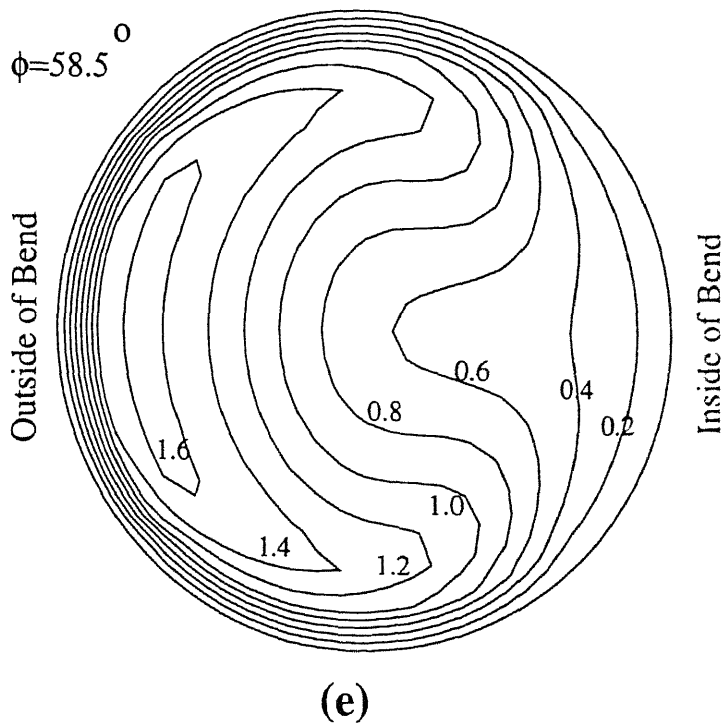


(c)

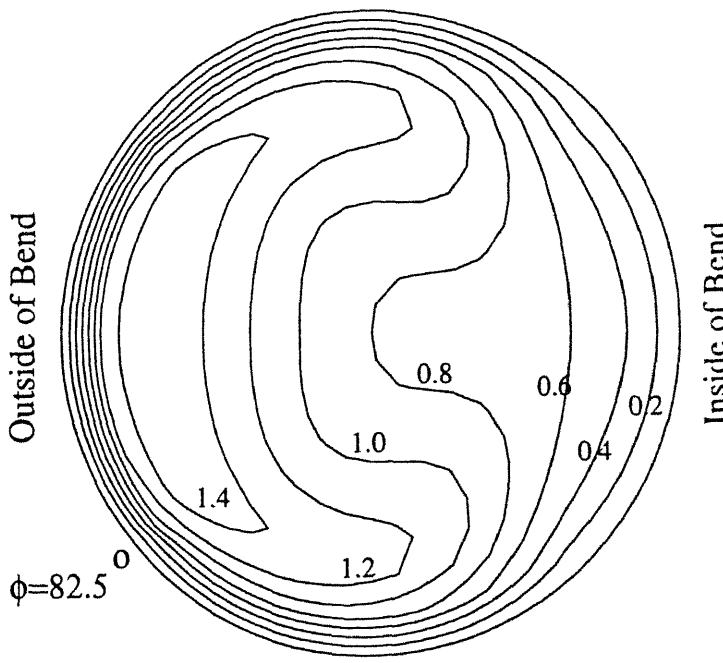


(d)

Figure 3.19: Development of the axial flow represented by isovelocity contours at (c) $\phi=22.5^{\circ}$, (d) $\phi=40.5^{\circ}$



(e)



(f)

Figure 3.20: Development of the axial flow represented by isovelocity contours at (e) $\phi=58.5^0$, (f) $\phi=82.5^0$

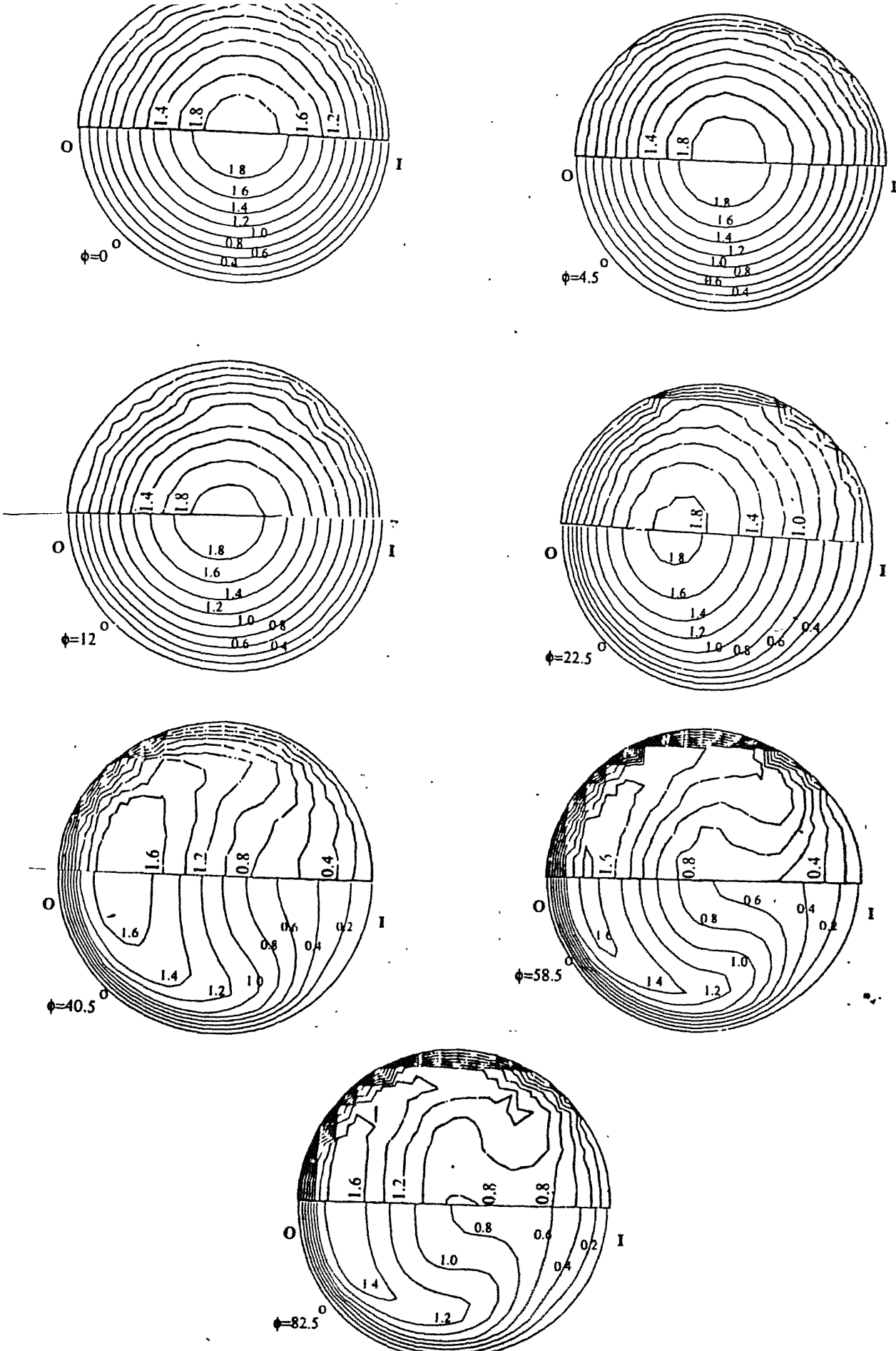


Figure 3.21: Comparison of the isovelocity contours between the present results and experimental[15]. The upper half domain corresponds to the experimental

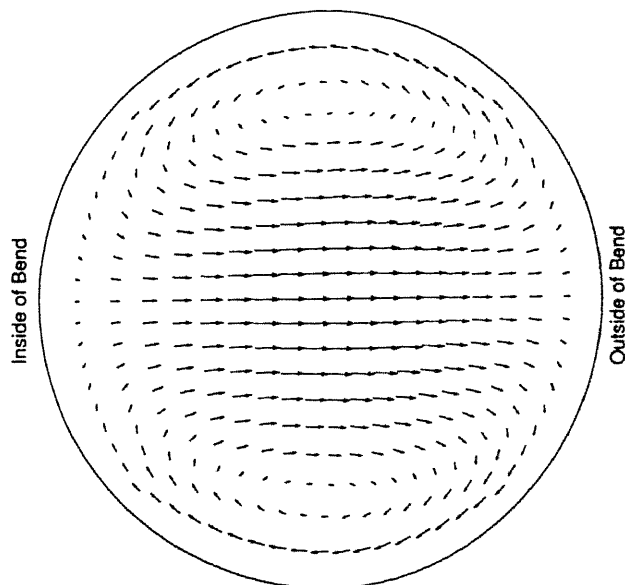
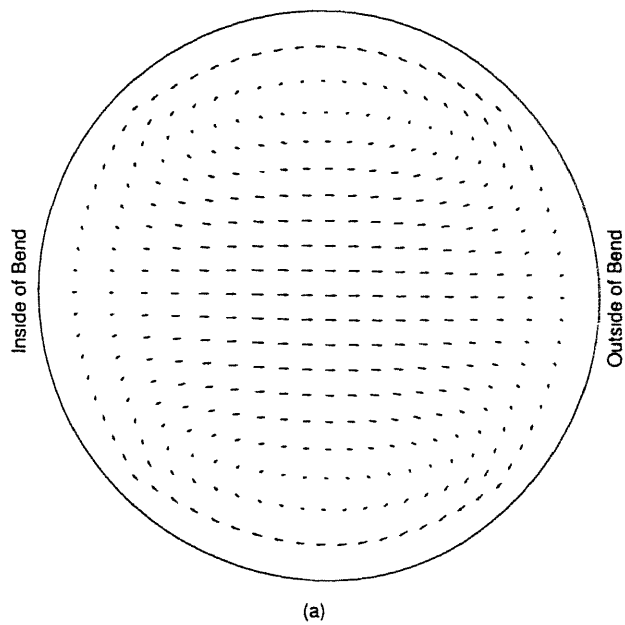
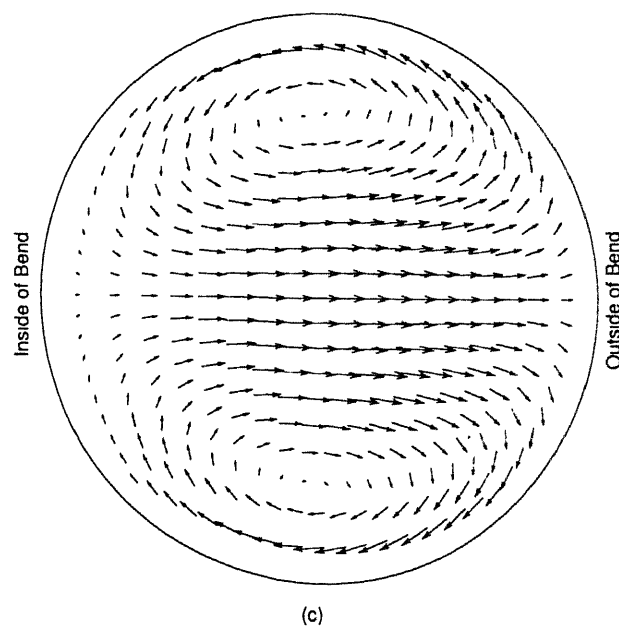
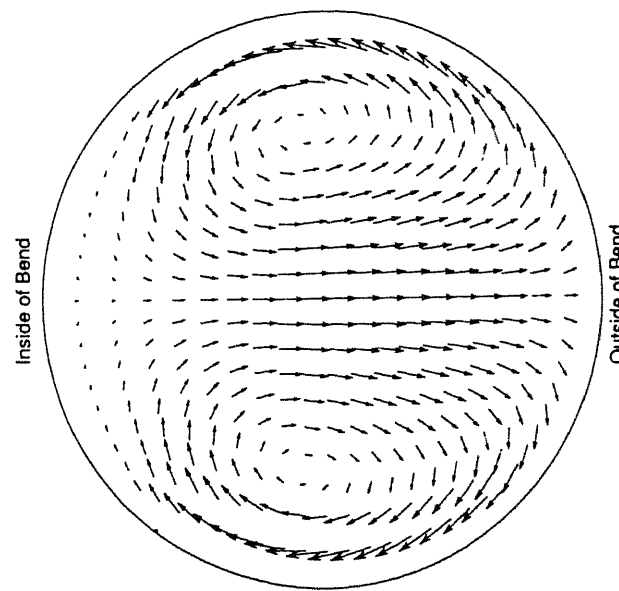


Figure 3.22: Development of secondary flow represented by vector plots at
(a) $\phi=4.5^{\circ}$, (b) $\phi=12^{\circ}$



(c)



(d)

Figure 3.23: Development of secondary flow represented by vector plots at
(c) $\phi=22.5^0$, (d) $\phi=40.5^0$

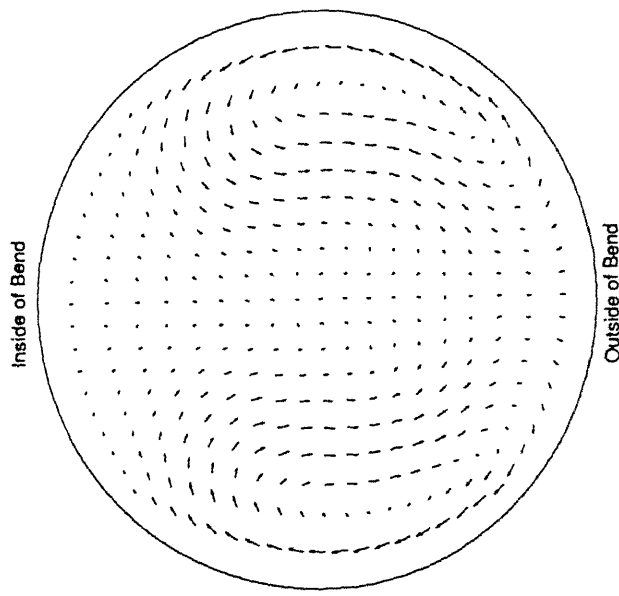
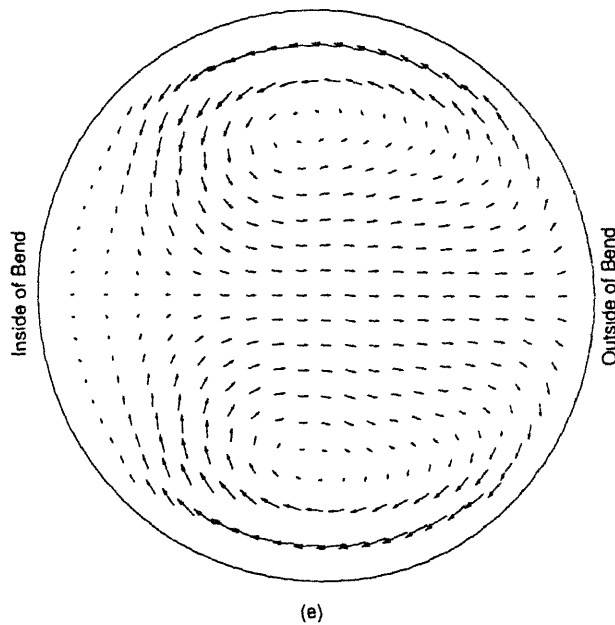


Figure 3.24: Development of secondary flow represented by vector plots at
(e) $\phi=58.5^0$, (f) $\phi=82.5^0$

Chapter 4

Conclusion

The general form finite volume Navier Stokes solver has been thoroughly tested for laminar flows in 2D and 3D regular geometries. The results for 3D flows in complex geometries are close to experimental results of established repute. Thus this thesis validates the accuracy and robustness of the Navier Stokes solver. Thus the solver has now been fully validated and may be used to study laminar and turbulent flows in complex flows.

Bibliography

- [1] Fletcher, C.A.J., *Computational techniques for fluid dynamics*, Vol.II, Springer Verlag, New York, 1988.
- [2] Baker, A.J., *Finite element computational fluid mechanics*, Hemisphere Publishing Corporation, New York, 1983.
- [3] Steger, J.L., and Sorenson. R.L., Automatic mesh point clustering near a boundary in grid generation with elliptic partial differential equations, *J. Comput. Phys.*, Vol. 33, pp. 405-410 (1979).
- [4] Sorenson, R.L., and Steger, J.L., Numerical generation of two dimensional grids by the use of poisson equations with grid control at boundaries. *Numerical grid generation techniques*, NASA Conf. Pub., 2166 (1980).
- [5] Thompson, J.F., Warsi, J.U.A.. and Mastin, C.W., Boundary fitted coordinate system for numerical solution of partial differential equations- A review, *J.Comput. Phys*, Vol. 47, pp. 1-108 (1982).
- [6] Rhie, C.M., and Chow, W.L., Numerical study of the turbulent flow past an aerofoil with trailing separation, *AIAA J.*, Vol. 21, pp. 1325-1332 (1983).
- [7] Eswaran, V., and Satya Prakash., Numerical simulation of unsteady 3-D flow around an elongated body moving in an incompressible fluid – ‘Validation of finite volume program’, Project report No.3 Submitted to DRDL, Hyderabad (1996).

- [8] Kordulla, W., and Vinokur. M., Efficient computation of volume in flow predictions, *AIAA Journal*, Vol. 21, pp. 917-918, (1983).
- [9] Khosla, P.K., and Rubin, S.G., A diagonally dominant second-order accurate implicit scheme, *Computers and Fluids*, Vol. 2, pp. 207-209, (1974).
- [10] Humphrey, J.A.C., Taylor, A.M.K.P., & Whitelaw, J.H., Laminar flow in a square duct of strong curvature, *Journal Of Fluid Mechanics*, Vol. 83, pp. 509-527 (1977).
- [11] Taylor, A.M.K.P., Whitelaw, J.H., & Yianneskis.M., Curved ducts with strong secondary motion: Velocity measurements of developing Laminar and turbulent flow, *Journal Of Fluids Engineering*, Vol. 104, pp. 350-359 (1982).
- [12] Ward-Smith, A.J., *Pressure losses in ducted flows*, Butterworths. (1971).
- [13] Kaushik, S., & Rubin, S.G., Incompressible Navier Stokes solutions with a new primitive variable solver, *Computers & Fluids*, Vol. 24, No.1, pp. 27-40 (1995).
- [14] Phille, P., Vehrenkamp, R., & Schulz-Dubois. E.O., The development and structure of primary and secondary flow in a curved square duct. *Journal of Fluid Mechanics*, Vol. 151, pp. 219-241 (1985).
- [15] Bovendeerd, P.H.M., Van Steenhoven, A.A., Van De Vosse, F.N., and Vossers, G., Steady entry flow in a curved pipe, *Journal of Fluid Mechanics*, Vol. 177, pp. 233-246, (1987).
- [16] Senthil, S., A study in two dimensional grid generation, M.Tech Thesis, IIT Kanpur, 1997.
- [17] Eswaran, V., and Senthil, S., Numerical simulation of unsteady 3D flow over an elongated body, 'Turbulence Modelling', Report No.4, Submitted to DRDL, Hyderabad (1998).

TH
ME/1998/M
J936-
A127940

127940

127940

This book is to be returned on the date last stamped.



A127940